Geophysical Journal International

Geophys. J. Int. (2015) **202,** 190–218 doi: 10.1093/gji/ggv130

GJI Seismology

Multiscale, finite-frequency *P* and *S* tomography of the upper mantle in the southwestern Fennoscandian Shield

Marianne L. Kolstrup,[1] Shu-Huei Hung[2] and Valerie Maupin[1]

[1]*Department of Geosciences, University of Oslo, N-0371 Oslo, Norway. E-mail: m.l.kolstrup@geo.uio.no*
[2]*Department of Geosciences, National Taiwan University, Taipei, Taiwan*

Accepted 2015 March 16. Received 2015 March 12; in original form 2014 September 22

SUMMARY

We image the *P*- and *S*-wave structure of the upper mantle in southwestern Scandinavia using a wavelet-based, multiscale parametrization and finite-frequency theory to model wave propagation. Relative traveltime residuals of direct *P* and *S* waves are measured in a high- and low-frequency band and are corrected for crustal structure using a detailed model for the study area. A range of resolution tests are used to find optimal damping values not only for variations in V_P and V_S separately, but also for perturbations in their ratio $V_\mathrm{P}/V_\mathrm{S}$. The tests show that features down to a size of 100 (150) km can be well resolved in the *P* (*S*) tomography. To ease comparison with previous studies we also perform ray-theoretical multiscale tomographies, and to test the degree of vertical smearing we evaluate different parametrizations in the vertical direction (wavelet-based multiscale and convolutional quelling). Our finite-frequency, multiscale images of variations in V_P and V_S confirm the existence of low velocities below southern Norway and Denmark and high velocities beneath the shield proper in Sweden, as seen in previous studies, but add more details to this simplified picture. The low velocities below southern Norway and Denmark are confined to a channel-like structure at about 100–200 km depth, and the lateral transition from low to high velocities follows zones of Carboniferous-Permian extension and magmatism very closely. A deeper low-velocity anomaly below central southern Norway emerges from the channel at 150 km depth and extends to a depth of 350 km. In the Swedish area we infer high-velocity anomalies in V_P and V_S, and negative anomalies in $V_\mathrm{P}/V_\mathrm{S}$ that indicate a strongly depleted mantle. We propose that the episodic erosion and convective removal of an originally thick mantle lithosphere below southern Norway to its current thickness of about 100 km could have been a trigger for episodic uplift in the Mesozoic and Cenozoic.

Key words: Body waves; Seismic tomography; Intra-plate processes; Cratons; Dynamics of lithosphere and mantle.

1 INTRODUCTION

Recent geophysical studies in the western Fennoscandian Shield have revealed a region of anomalously low seismic velocities in the uppermost mantle below southern Norway compared to the otherwise high velocities of the Fennoscandian Shield mantle (Weidle & Maupin 2008; Maupin 2011; Medhus *et al.* 2012; Wawerzinek *et al.* 2013). The general picture of a low-velocity anomaly and a transition to the Fennoscandian Shield is present in all studies, but different seismic models show differences in amplitude and location of the anomaly (Medhus *et al.* 2012; Wawerzinek *et al.* 2013) that have not been explained.

The low-velocity anomaly grossly coincides with the high topography in southern Norway, which has an unknown and highly debated origin (e.g. Lidmar-Bergstrom & Bonow 2009; Nielsen *et al.* 2009a,b; Gabrielsen *et al.* 2010). It is in particular important to ascertain whether the low-velocity upper mantle contributes to the isostatic compensation of the high topography (e.g. Pascal & Olesen 2009; Ebbing *et al.* 2012; Medhus *et al.* 2012; Gradmann *et al.* 2013). A robust estimate of the magnitude and location of the low-velocity anomaly and the transition to the Fennoscandian Shield proper is therefore crucial.

The Fennoscandian Shield contains an Archean core (3.7–2.6 Ga) in the northeast and progressively younger domains towards the southwest (Gaál & Gorbatschev 1987) that accreted to the Archean core in the Palaeoproterozoic (e.g. Gaál & Gorbatschev 1987; Nironen 1997; Högdahl *et al.* 2004). The study region (Fig. 1) covers most of the youngest part of the Fennoscandian Shield in the southwest (Gaál & Gorbatschev 1987), which is mainly the product of Mesoproterozoic continental growth (Gaál & Gorbatschev 1987; Bingen *et al.* 2005) and late Mesoproterozoic deformation in the Sveconorwegian Orogeny (1.25–0.90 Ga, Gaál & Gorbatschev

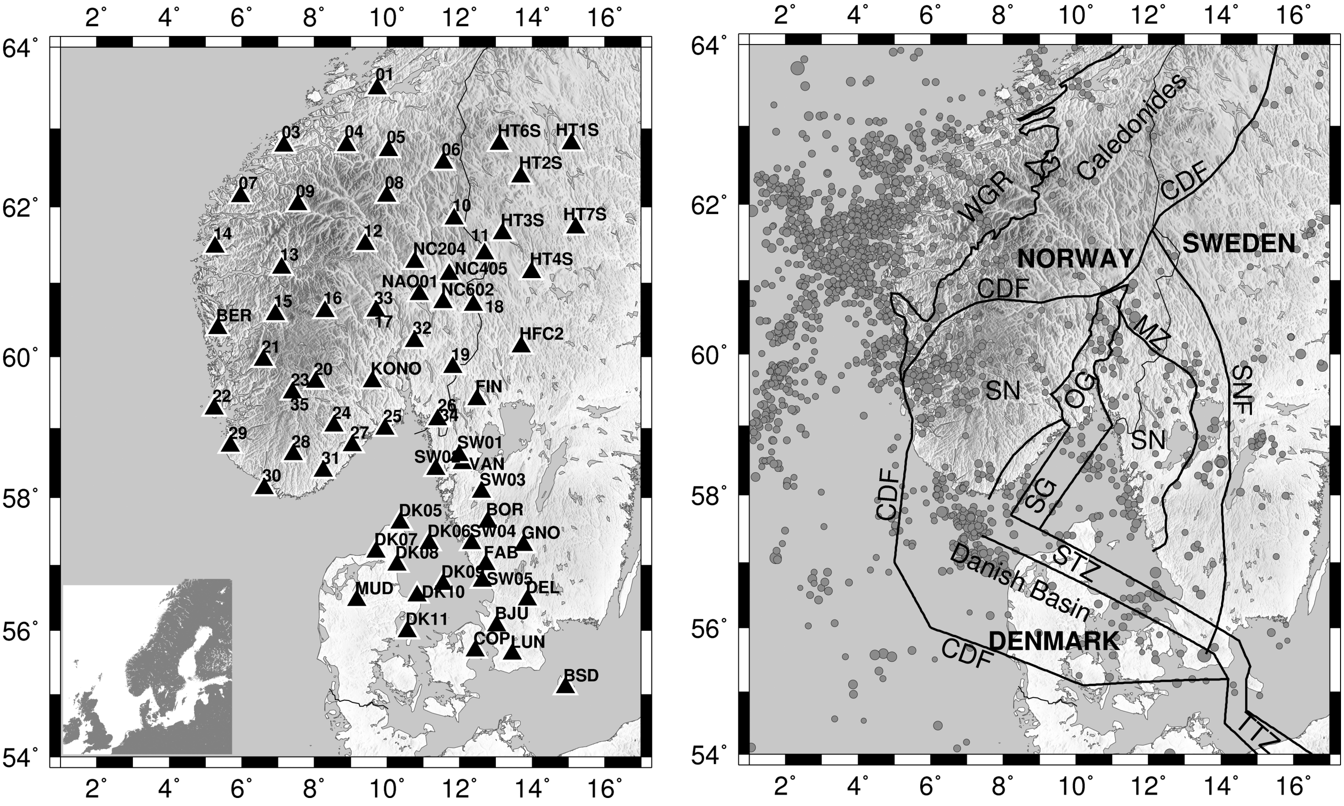

Figure 1. Station network and tectonic overview of the study region. Left: Seismological stations with topography and a regional map in the lower left corner. Numbers xx are abbreviations of the MAGNUS station names NWGxx. Right: Major tectonic features with topography and seismic events from 1980 to 2011 with $M \geq 2.0$ (FENCAT 2011). CDF, Caledonian front; MZ, Mylonite Zone; OG, Oslo Graben; SG, Skagerrak Graben; SN, Sveconorwegian; SNF, Sveconorwegian front; STZ, Sorgenfrei-Tornquist Zone; TTZ, Teisseyre-Tornquist Zone; WGR, Western Gneiss Region.

1987). The southern part of the study area was created by the docking of the microcontinent Avalonia (440 Ma), and the later Caledonian Orogeny (420–400 Ma) (Roberts 2003; Cocks & Torsvik 2006) that also heavily deformed the northwestern part. The last major tectonic events in the study region were the late Carboniferous-Permian rifting with extension and magmatism in the Oslo and Skagerrak Grabens and along the Sorgenfrei-Tornquist Zone (305–220 Ma, Neumann *et al.* 2004; Larsen *et al.* 2008) and formation of the Danish Basin (Sørensen 1986; Frederiksen *et al.* 2001) before the North Atlantic breakup $\sim$55 Ma.

Regional tomographies based on Rayleigh wave dispersion or full-waveform inversion covering our study area (Weidle & Maupin 2008; Rickers *et al.* 2013) infer V_{SV} and V_{SH} velocities 6 per cent lower than in AK135 (Kennett *et al.* 1995) below southern Norway and high velocities below neighbouring Sweden. Local studies drawing on surface waves (Maupin 2011; Köhler *et al.* 2012) infer V_{SV} velocities 2–3 per cent lower than AK135 (Kennett *et al.* 1995). New tomographies of Europe using full waveform inversion (Zhu *et al.* 2012, 2013; Fichtner *et al.* 2013) invert jointly for V_{Φ}, V_{SH} and V_{SV} and cover our study area, but do not provide enough details on a local scale to accurately image the lateral variations in the western Fennoscandian lithosphere.

The regional *P*- and *S*-wave tomographies in the area (Medhus *et al.* 2012; Wawerzinek *et al.* 2013) have better resolution than the surface waves studies but generally lower amplitudes. The relative V_{S} anomalies in the ray-based tomography of Wawerzinek *et al.* (2013) are up to ± 1.5 per cent, an amplitude similar to the one found for V_{P} velocities in Medhus *et al.* (2012). It is not clear whether this similarity in magnitude stems from an actual similarity in nature, or from a higher degree of smoothing in the *S*-wave tomography.

The preservation of amplitudes of velocity anomalies is critical when it comes to the tectonothermal interpretation of tomographies. As seismic velocities are more sensitive to temperature than to composition (e.g. Goes *et al.* 2000; Cammarano *et al.* 2003), velocity anomalies are usually interpreted as temperature anomalies. Below southern Norway the velocity anomaly measured with surface waves has been interpreted as a temperature anomaly of about 200 °C (Maupin 2011; Maupin *et al.* 2013), but integrated petrological modelling suggest that a difference in composition is also needed to explain the transition from low to high seismic velocities (Gradmann *et al.* 2013). The $V_{\mathrm{P}}/V_{\mathrm{S}}$ ratio is often used as a diagnostic of compositional anomalies (e.g. Lee 2003; Artemieva 2007) but we cannot access this ratio from tomographies of V_{P} and V_{S} derived using different parametrizations and regularizations, as tomographic images are non-unique and strongly dependent on the choice of regularization (Trampert & Snieder 1996; Chiao & Liang 2003; Chiao *et al.* 2010).

We wish to close the gap between local relative traveltime tomography and regional full-waveform inversion and present in this study tomographic models of V_{P} and V_{SH} that can be compared quantitatively. The models are derived using a wavelet-based multiscale parametrization combined with finite-frequency theory to model wave propagation (Hung *et al.* 2010, 2011) and a finite-frequency data set of traveltime residuals from Kolstrup (2015).

Traveltimes measured in multiple frequency bands are sensitive to heterogeneities at different spatial scales and hence increase the amount of information available for each source–receiver pair in the data set, giving better recovery of the magnitude of velocity anomalies in tomographic models (Hung *et al.* 2004; Sigloch 2008). Multiscale parametrizations based on wavelet transforms (Chiao & Kuo 2001; Chiao & Liang 2003; Chevrot & Zhao 2007; Loris *et al.* 2007; Charléty *et al.* 2013) are data adaptive and preserve the long-wavelength amplitude spectra in sparsely sampled regions without losing resolution in densely covered regions. This is an advantage compared to using a detailed local parametrization, for example blocks as often used in regional body wave tomography, which emphasizes spatial resolution but reduces the magnitude of long-wavelength anomalies through the high need of smoothing regularization.

We outline the main features of multiscale, finite-frequency tomography in Section 3, after a summary of the data sets (Section 2). Preferred tomographic models are presented in Section 4.1 and followed by extensive tests of the results (Sections 4.2–4.5). We discuss our findings in relation to thermal and dynamic modelling of the area and the current debate about the origin of the Scandinavian Mountains (Section 5).

2 DATA

The data used in this study were recorded by the temporary MAGNUS network between 2006 September and 2008 June (Weidle *et al.* 2010), by the temporary DANSEIS network from 2008 April to 2008 June, by the temporary CALAS stations (Medhus *et al.* 2009), and by permanent stations in the study area (Fig. 1).

The data examined come from earthquakes with magnitude $M > 5.0$ that occurred at epicentral distances of 30 to 91.5° (Fig. 2). Most events occurred at distances greater than 70°, making the separation of phases like *P*(S) and *PcP* (*ScS*) difficult and giving a weak *PcP* (*ScS*) signal (Kolstrup 2015). Therefore, only the direct *P* and *S* phases are included in the data set for the tomography.

P waves are measured on the vertical component of the seismograms and *S* waves are measured on the transverse component. The data are bandpass filtered using different second-order, zero-phase Butterworth filters. For *P* waves, the high- and low-frequency bands are 0.3–0.125 Hz (33–8 s) and 0.5–2 Hz (2–0.5 s), respectively. This isolates the secondary noise peak at around 0.2 Hz (5 s) in southern Norway. *S* waves are bandpass filtered in the ranges 0.03–0.077 Hz (33–13 s) and 0.077–0.125 Hz (13–8 s). Due to the relatively high noise level above 0.125 Hz (8 s), it was not possible to measure higher frequency *S* waves, as also found by Wawerzinek *et al.* (2013). Traveltimes are measured using an automated processing procedure tailored for measuring traveltimes in several frequency bands (Kolstrup 2015). The multichannel cross-correlation method (MCCC) of VanDecar & Crosson (1990) is preceded by several steps of automatic data rejection and by a preliminary picking of arrival times using the iterative cross-correlation and stack algorithm (ICCS) of Lou *et al.* (2013).

The multichannel cross-correlation method measures all relative delays between stations Δt_{ij} and solves in a least-squares sense for the optimized arrival times t_i at each station under a constraint of $\sum t_i = 0$. This implies that the measured traveltimes are relative to the mean traveltime for each event, removing uncertainty regarding source location and timing (VanDecar & Crosson 1990) but also removing information about absolute velocities in the study region.

The relative arrival times are then transformed to traveltime residuals by subtracting demeaned theoretical arrival times calculated in the spherically symmetric, continental earth model AK135 (Kennett *et al.* 1995). The traveltime residuals are corrected for the ellipticity of the Earth and for variations in topography and crustal structure (Kennett & Gudmundsson 1996; Euler 2014; Kolstrup 2015) using a detailed crustal model based on information from a wide range of sources and compiled in Kolstrup (2015). Especially useful for the crustal corrections are the Moho depths and *S*-wave velocity

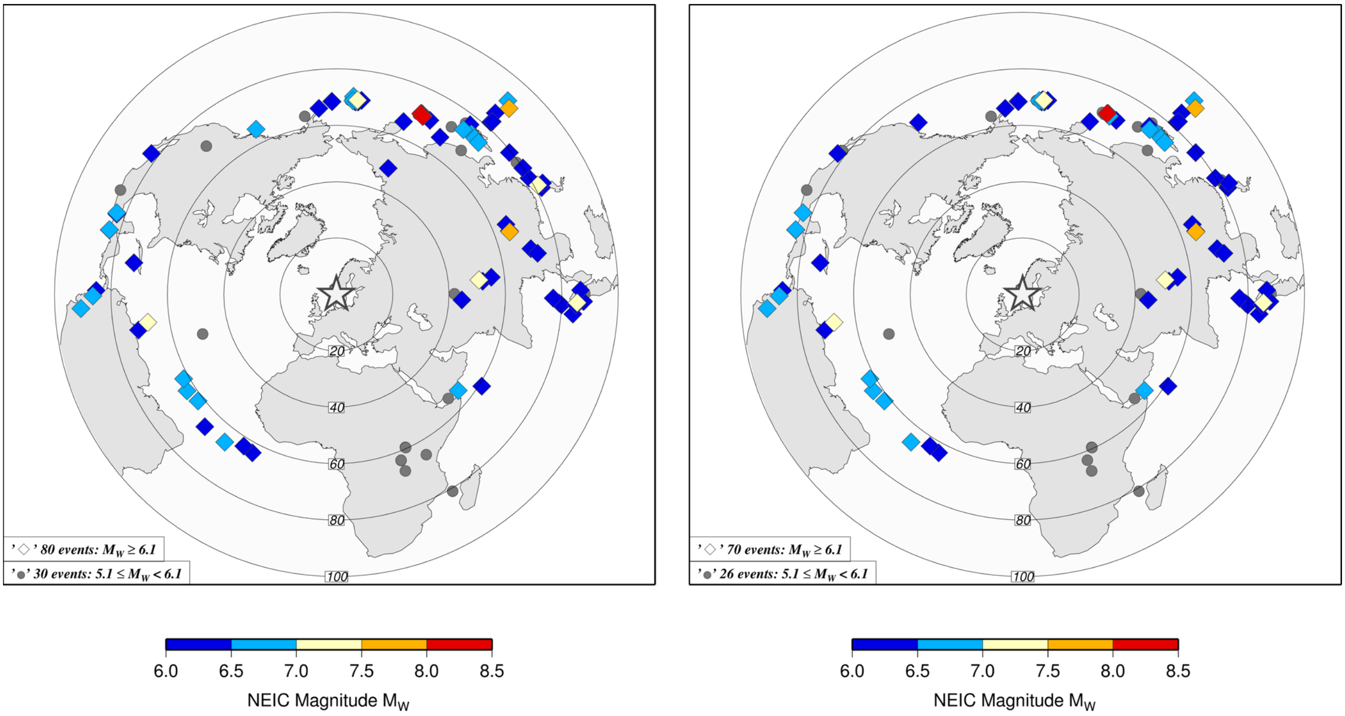

Figure 2. Map of earthquake sources used in the tomographies. The events displayed have given traveltime data in at least one frequency band. Left: Events used in the *P*-wave tomography. Right: Events used in the *S*-wave tomography.

models from joint inversion of *P*-receiver functions and surface waves (Kolstrup & Maupin 2013) beneath the temporary Magnus stations and beneath permanent stations in Norway and Sweden, as these models give information directly beneath the stations with no need for interpolation.

The crustal corrections are performed using ray theory and are therefore equal for both high and low-frequency bands. It is well-established that crustal reverberations cause a significant difference between traveltimes of long- and short-period waves that must be taken into account in global absolute traveltime tomography (Obayashi *et al.* 2004; Yang & Shen 2006; Ritsema *et al.* 2009). For regional relative tomography, though, the data are demeaned in each frequency band and it is therefore only the relative variation of crustal traveltimes in the study region that is important (Maupin & Kolstrup 2015, in revision). Ray-theoretical corrections in some cases overestimate the influence of the crust on low-frequency traveltimes (Maupin & Kolstrup 2015, in revision), and we therefore also invert for a tomographic model without crustal corrections (Section 4.3).

The resulting data set consists of 4205 and 3927 direct *P* arrivals in the high and low-frequency bands, respectively, from 110 events (Fig. 2). For *S* waves, the corresponding numbers are 3766 and 3187, from 96 events (Fig. 2).

Fig. 3 shows map views of *P*-wave traveltime residuals from opposite backazimuths, corrected for crustal structure and ellipticity of the Earth. The residuals are calculated for each station as weighted averages of all residuals from the northeastern and southwestern quadrants, respectively, using the inverse of the estimated standard deviations in measurement error (VanDecar & Crosson 1990) as weights.

The high-frequency residuals from the northeastern quadrant (Fig. 3a) show a simple, almost bimodal, picture of early residuals in the east and late residuals in the west, whereas the high-frequency residuals from the southwestern quadrant (Fig. 3c) are early in both the southwestern and easternmost areas. This indicates a more complicated 3-D subsurface structure than suggested by the northeastern residuals, with the presence of high velocities off coast southwestern Norway.

The *P*-wave residuals from the lower frequency bands do not differ in magnitude from the higher frequency residuals, but differ in the spatial distribution of positive and negative residuals (Figs 3b and d), especially in the southern part of the of the study area where the long-period waves are less sensitive to the presence of sedimentary layers (Maupin & Kolstrup 2015, in revision). For events from the southwestern quadrants the changed pattern in negative residuals in the southwestern areas suggest the presence of a high velocities off coast western Denmark that are sensed by the lower frequency residuals due to their broader kernels. Hence, providing data from several frequency bands clearly increases the amount of information about subsurface structure and calls for finite-frequency tomography.

3 THEORY AND METHOD

Multiscale, finite-frequency tomography was described in detail by Hung *et al.* (2011) and we only review the main points and features important for our results.

The basis of linearized traveltime tomography is the formulation

$$\delta t = \iiint_{\oplus} K(\boldsymbol{x})\delta s(\boldsymbol{x})\mathrm{d}^3\boldsymbol{x}, \qquad (1)$$

where δt is the observed traveltime residual with respect to given spherically symmetric, standard earth model, and $K(\boldsymbol{x})$ is the sensitivity kernel that relates δt to perturbations in *P*- or *S*-wave slowness $s(\boldsymbol{x})$ at every point $\boldsymbol{x}$ in the region $\oplus$. To construct the kernels $K(\boldsymbol{x})$ we use the finite-frequency theory developed by Dahlen *et al.* (2000) in which the Born approximation for forward scattering is combined with ray theory for body waves and the paraxial approximation for wavefronts away from the central ray.

As mentioned in Section 2, the traveltime residuals δt are demeaned for each event. This implies that the appropriate kernel for a relative traveltime measurement is the one associated with this particular source-station path minus the average kernel for all the data from this particular source (e.g. Chevrot & Zhao 2007). For most network configurations though, the difference between the usual kernels and the relative ones is small enough not to bias the tomography (Maupin & Kolstrup 2015, in revision). Another effect of the demeaning is that the model inverted from the relative traveltime residuals will be relative to the unknown 1-D average model of the study region (Aki *et al.* 1977).

The seismic network used in this study covers an area of approximately 500 km by 800 km and is discretized into a grid of 65 ($2^6 + 1$) by 65 ($2^6 + 1$) by 33 ($2^5 + 1$) (=139 425) nodes with a grid spacing of 25 km and until a depth of 800 km. Even though we correct the traveltime residuals for crustal structure, we include two layers in the crust and upper mantle at 0–25 and 25–50 km, as crustal corrections are never perfect (Martin *et al.* 2005; Maupin & Kolstrup 2015, in revision) and the model most be free to account for those imperfections in the uppermost layers.

Numerical integration of the kernels $K(\boldsymbol{x})$ around each node leads to a data equation that relates the slowness perturbation at each node to the traveltime measurements:

$$\boldsymbol{d} = \boldsymbol{G}\boldsymbol{m}, \qquad (2)$$

where $\boldsymbol{d}$ is the data vector containing the N traveltime measurements δt_i and $\boldsymbol{m}$ is the model vector containing the M (139 425) slowness parameters. The elements $\boldsymbol{G}_{ij}$ of the matrix $\boldsymbol{G}$ represents the sensitivity of the ith datum with respect to the slowness perturbation at the jth node.

Instead of solving eq. (2) directly for the model parameters $\boldsymbol{m}$, using regularizations like norm damping and smoothing, the multiscale parametrization expands the model parameters $\boldsymbol{m}$ in terms of wavelet basis functions in 3-D (e.g. Chiao & Kuo 2001; Chevrot & Zhao 2007; Hung *et al.* 2011), giving an equation similar to eq. (2), but with both $\boldsymbol{G}$ and $\boldsymbol{m}$ transformed into wavelet space, utilizing the CDF (2,2) wavelet (Cohen *et al.* 1992) and the lifting scheme (Sweldens 1996). This decomposes the model into a hierarchy of wavelet coefficients at various scales, with up to six scale-levels of successive refinements. The coarsest level (=1) is at a length-scale of the entire domain and the finest level (=6) is at a length-scale of the grid spacing (25 km).

Hence, the model parameters that are inverted for, using weighted, damped least-squares solution (DLS; e.g. Menke 1984), are wavelet coefficients associated with each grid node. Minimum norm damping (ℓ_2 norm) in the DLS solution therefore acts on the wavelet coefficients and at several scale levels at a time, instead of uniformly on the entire model. This has the desirable effect that the finest scales being resolved are spatially varying, minimizing the need for regularization through *a priori* information, and preserving the amplitudes of long wavelength structures to a larger degree than conventional grid-based parametrizations (Chiao & Kuo 2001; Hung *et al.* 2011).

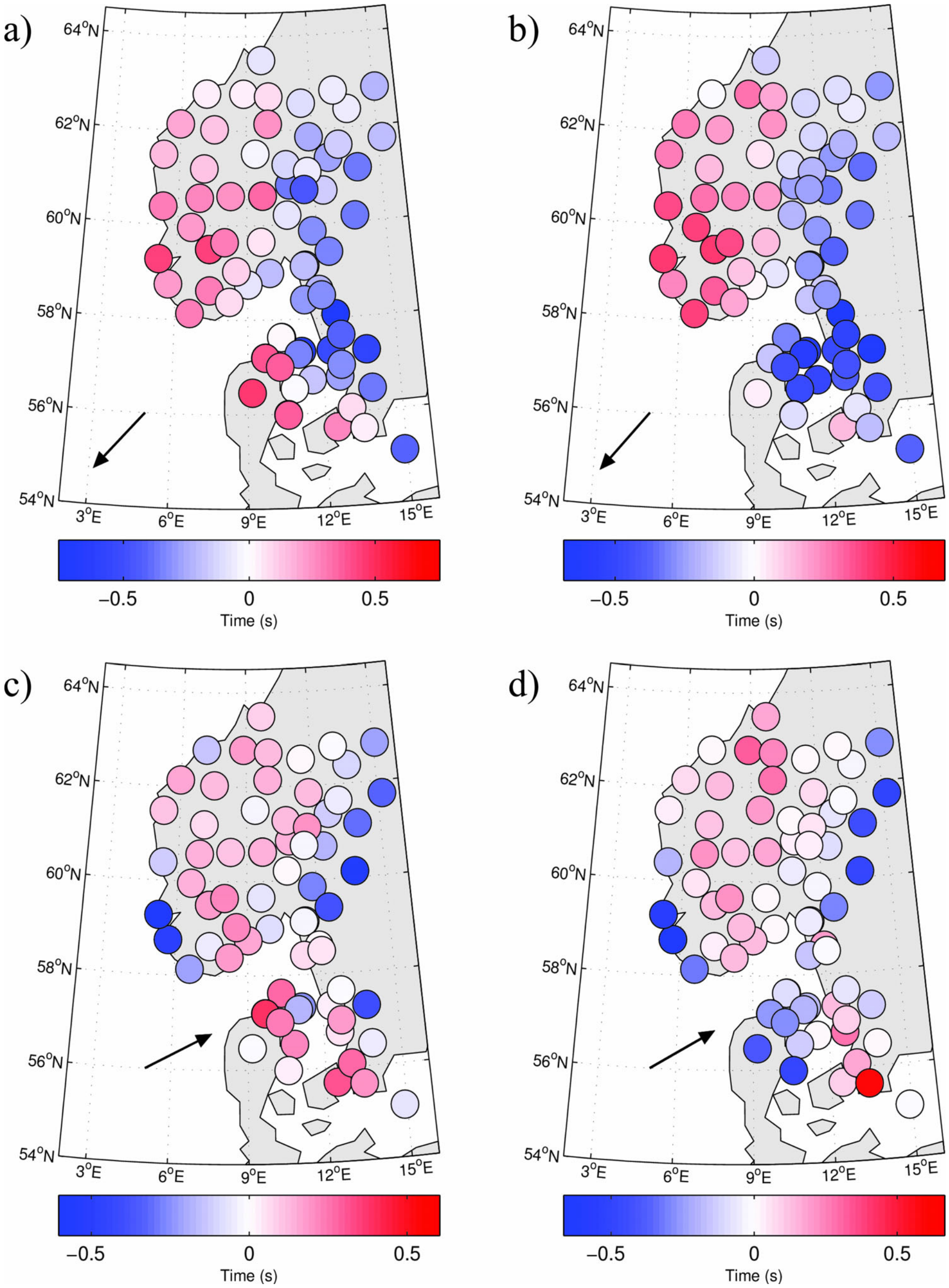

Figure 3. Average *P*-wave traveltime residuals from the northeastern and southwestern quadrants. The arrow shows the direction of the incoming wave. (a) High-frequency residuals from the northeastern quadrant. (b) Low-frequency residuals from the northeastern quadrant. (c) High-frequency residuals from the southwestern quadrant. (d) Low-frequency residuals from the southwestern quadrant.

The conventional ℓ_2 norm is used in the DLS-solution as it allows for convenient linearization of the inversion problem, but recent work suggests that the use of the ℓ_1 norm on wavelet coefficients gives a sparser and hence more robust solution (Loris *et al.* 2007; Charléty *et al.* 2013) that better recovers sharp discontinuities in the model. In a later work, Loris *et al.* (2010) performed more realistic synthetic experiments where the classic ℓ_2 norm penalty on the Laplacian of the model (smoothing) worked almost as well or even better than some of the ℓ_0- and ℓ_1-wavelet methods. The proper choice of wavelet transformation and regularization strategy therefore seems to be dependent on the target of the study (Loris *et al.* 2010), being for example recovery of amplitudes or sharpness of boundaries, and is an ongoing field of research (Simons *et al.* 2011; Chevrot *et al.* 2012; Charléty *et al.* 2013; Yuan & Simons 2014).

4 RESULTS

4.1 Images of $\delta\, lnV_{\mathrm{P}}$, δlnV_{S} and $\delta ln(V_{\mathrm{P}}/V_{\mathrm{S}})$

Preferred models of δlnV_{P} ($=\delta V_{\mathrm{P}}/V_{\mathrm{P}}$) and δlnV_{S} ($=\delta V_{\mathrm{S}}/V_{\mathrm{S}}$) are shown in map views in Figs 4 and 5, respectively, and in four profiles across the study region in Figs 6 and 7.

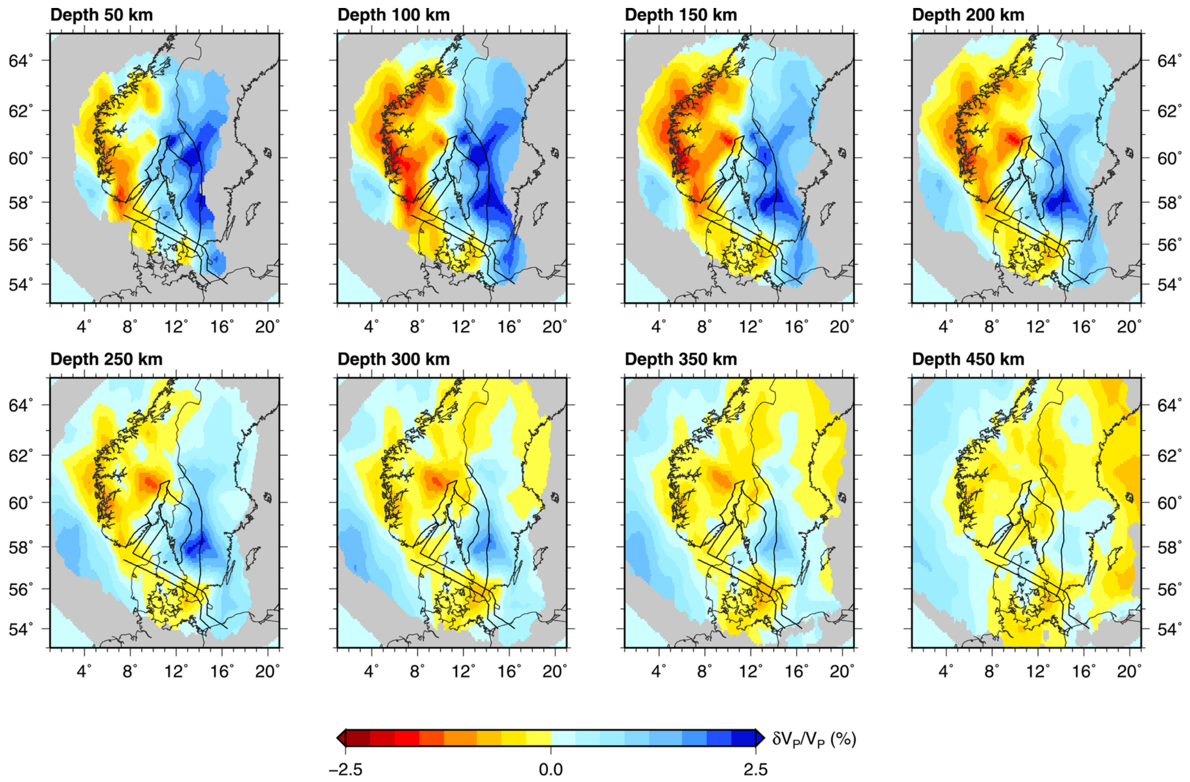

Figure 4. Map views of δlnV_P from at depths from 50 to 450 km derived using the full 3-D multiscale parametrization. Deep crustal structures from Fig. 1 are drawn with solid black lines (Mylonite Zone, Oslo and Skagerrak Grabens, Sorgenfrei-Tornquist Zone, Sveconorwegian Front, and Teisseyre-Tornquist Zone). Regions with poor resolution have been masked out.

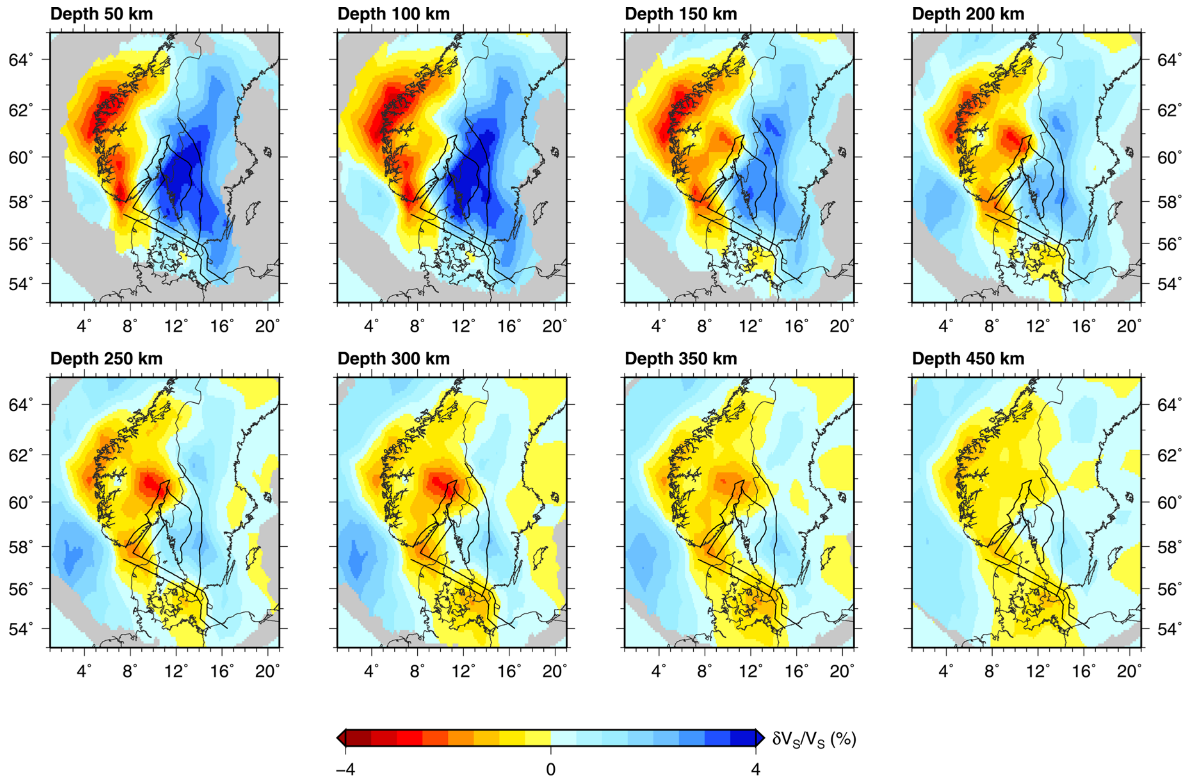

Figure 5. The same as Fig. 4 for δlnV_S.

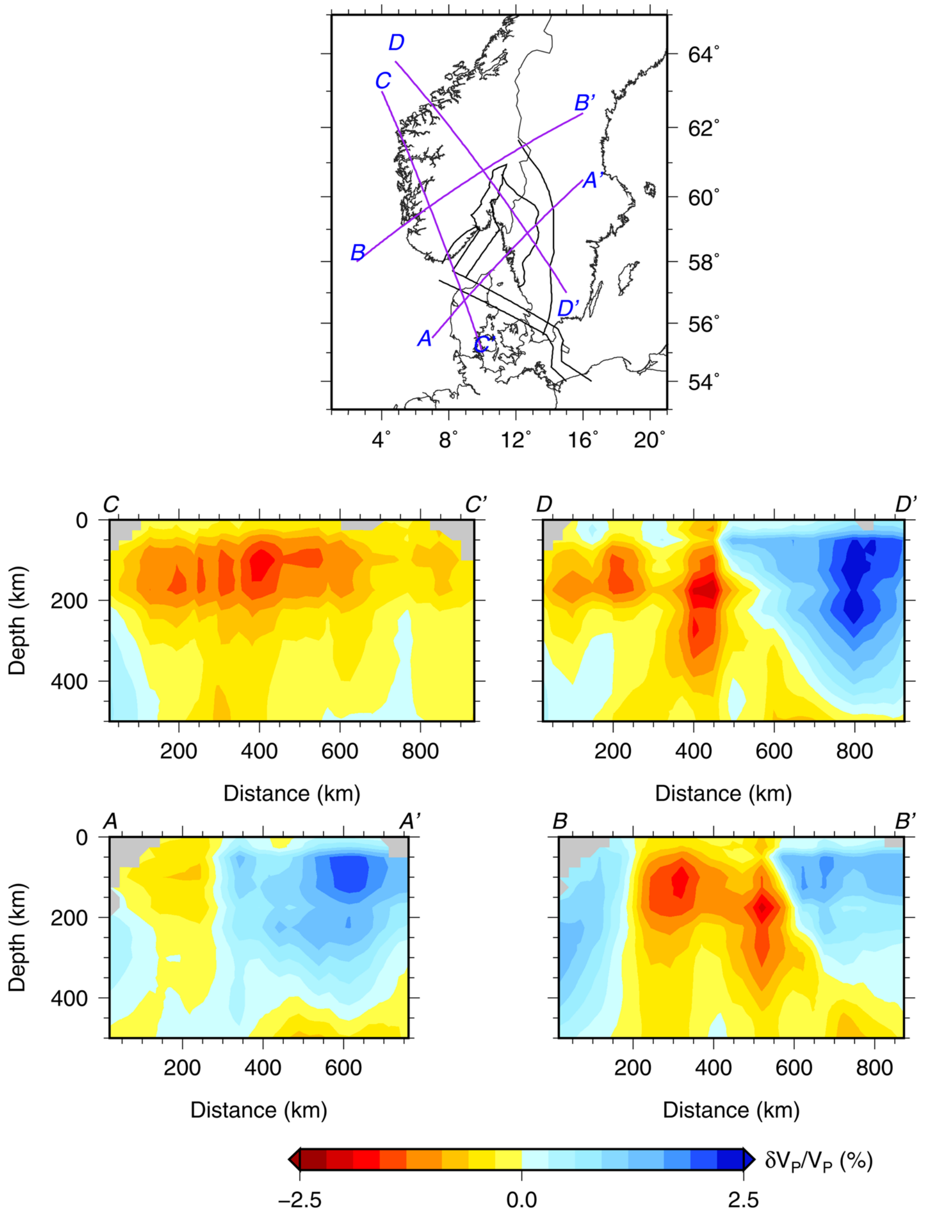

Figure 6. Profiles of δlnV_P derived using the 3-D multiscale parametrization. Regions with poor resolution have been masked out.

To visualize regions that are well sampled by the data, we plot the square root of the diagonal elements of the matrix $\boldsymbol{G}^T\boldsymbol{G}$, where $\boldsymbol{G}^T$ is the transpose of the matrix $\boldsymbol{G}$ in eq. (2). $\boldsymbol{G}^T\boldsymbol{G}$ is used as a proxy for the resolution matrix, as each of its diagonal elements is associated with a grid node and is the squared sum of the sensitivity kernels that contribute to this node. Comparison of the $\boldsymbol{G}^T\boldsymbol{G}$ images (Fig. 8) with resolution tests (Section 4.4) indicates that robustly constrained regions have $\boldsymbol{G}^T\boldsymbol{G}$ values exceeding 0.5 per cent of the overall maximum at all nodes, and that the data provide reliable images down to a depth of approximately 500 km for P and 400–500 km for S. In all images we do not display the model at nodes with a value below the threshold of 0.5 per cent (Figs 4–7).

The most striking structure of the models is a low-velocity region extending from western Norway to Denmark, strongest in the uppermost layers at depths between 100 and 200 km. Higher velocities are found both west and east of this region, and the low-velocity anomaly therefore has a horizontal, channel-like appearance. The channel seems to be adjacent to, and distinct from, a more circular anomaly below the northwestern end of the Oslo Graben, which extends deeper down to 350 km. The high-velocity area inferred off coast southwestern Norway and Denmark is present in both the P- and S-wave images and was predicted already from the raw data (Section 2). In the eastern part of the study area, high velocities extend from north to south and until a depth of around 300–350 km. The highest V_P anomalies of +2.5 per cent are found east of the Sveconorwegian Mylonite Zone, while the high V_S anomalies of up to +4 per cent are distributed more uniformly in the Sveconorwegian and Svecofennian areas (Fig. 1).

The wiggly boundary between the high velocities in the east and low velocities in the west has a steep, almost vertical angle in the southern part between Denmark and Sweden, and is more gently dipping between Norway and Sweden in the northern part (Figs 6 and 7). The boundary follows the Sorgenfrei-Tornquist Zone very closely in southern Sweden and Denmark and continues along the west side of the Skagerrak and Oslo Grabens before it terminates

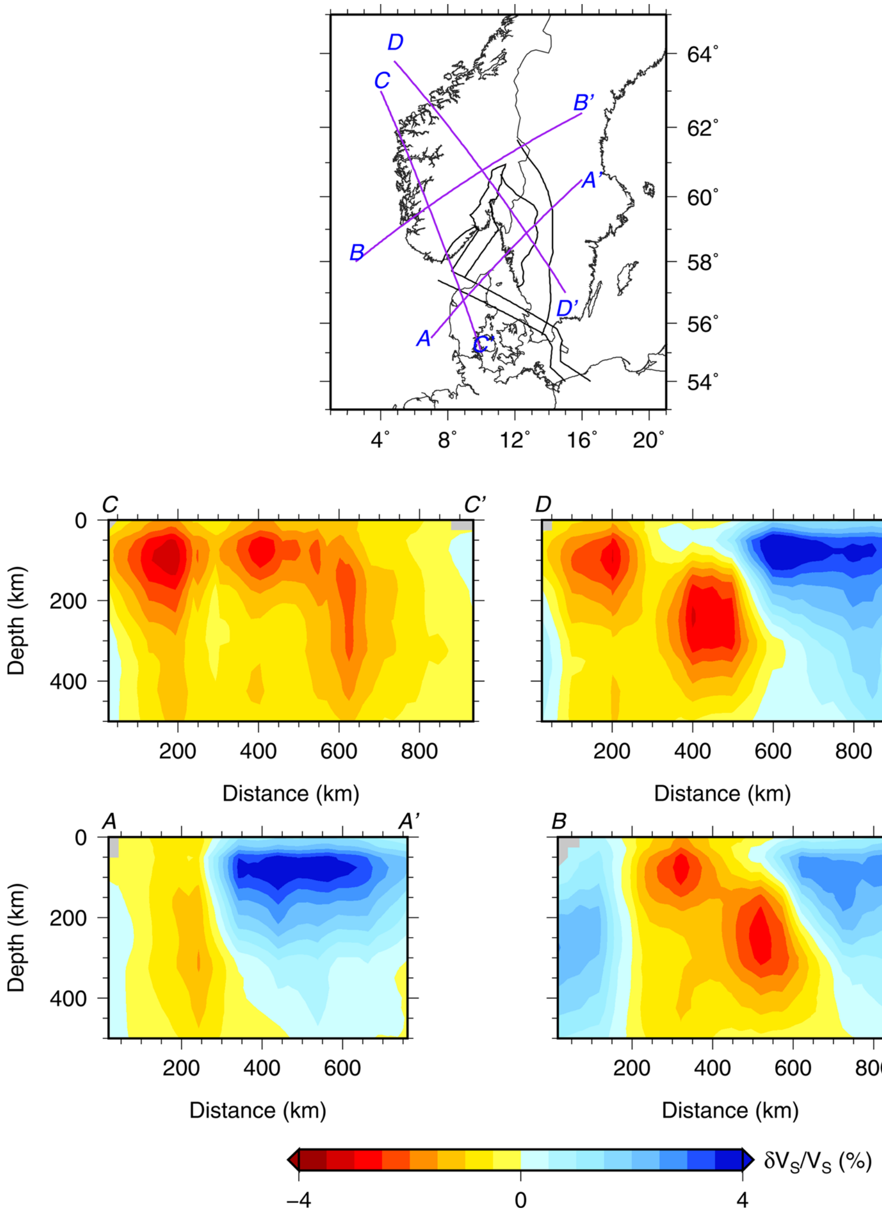

Figure 7. The same as Fig. 6 for $\delta ln V_S$.

in the northern part of the study area with no association to major tectonic structures (Fig. 1).

The *P*- and *S*-wave images are very similar in all features but the magnitude of the anomalies, which is larger for *S* as expected (e.g. Kennett *et al.* 1998; Goes *et al.* 2000). The amplitude variations are around -2.0 and $+2.5$ per cent for *P* waves and around -3.5 and $+4.0$ per cent for *S* waves. The *S*-wave models also appear slightly more smooth, possibly due to the longer wavelength of the *S*-wave data.

In order to compare the images of $\delta ln V_P$ and $\delta ln V_S$ quantitatively we calculate the perturbations in the ratio V_P/V_S, that is $\delta ln(V_P/V_S) = \delta ln V_P - \delta ln V_S$ (Fig. 9; e.g. Chou *et al.* 2009). The ratio V_P/V_S is often used as a diagnostic of compositional anomalies (Lee 2003; Artemieva 2007; Afonso *et al.* 2010), and it is therefore more straightforward to compare $\delta ln(V_P/V_S)$ to petrological results than the ratio $\delta ln V_P/\delta ln V_S$. In addition, $\delta ln(V_P/V_S)$ is more stable in numerical computations (Chou *et al.* 2009).

A consistent data set of common source–receiver pairs is usually preferred when computing V_P/V_S-ratios from tomographies (Chou *et al.* 2009; Hung *et al.* 2011) or when jointly inverting *P*- and *S*-wave data sets (Kennett *et al.* 1998). In our study we keep all available data to compute $\delta ln(V_P/V_S)$, as the event coverage is almost equal for the two data sets (Fig. 2) and evaluation of the resolution matrix proxy $G^T G$ shows comparable data coverage for the *P*- and *S*-wave tomographies (Fig. 8). In addition, equal source–receiver combinations do not guarantee compatibility of the *P* and *S* models as the wavelengths and kernels of the *P*- and *S*-wave data sets are anyway different for the two wave types and result in different resolutions. The perturbations in V_P/V_S are quite sensitive to small-scale variations in the models and it is important not to interpret underdamped solutions or regions of the images with low resolution (Hung *et al.* 2011). We use therefore a stronger cut off criteria of 1 per cent for the square root values of the diagonal elements of $G^T G$ in the plots of $\delta ln(V_P/V_S)$ (Fig. 9).

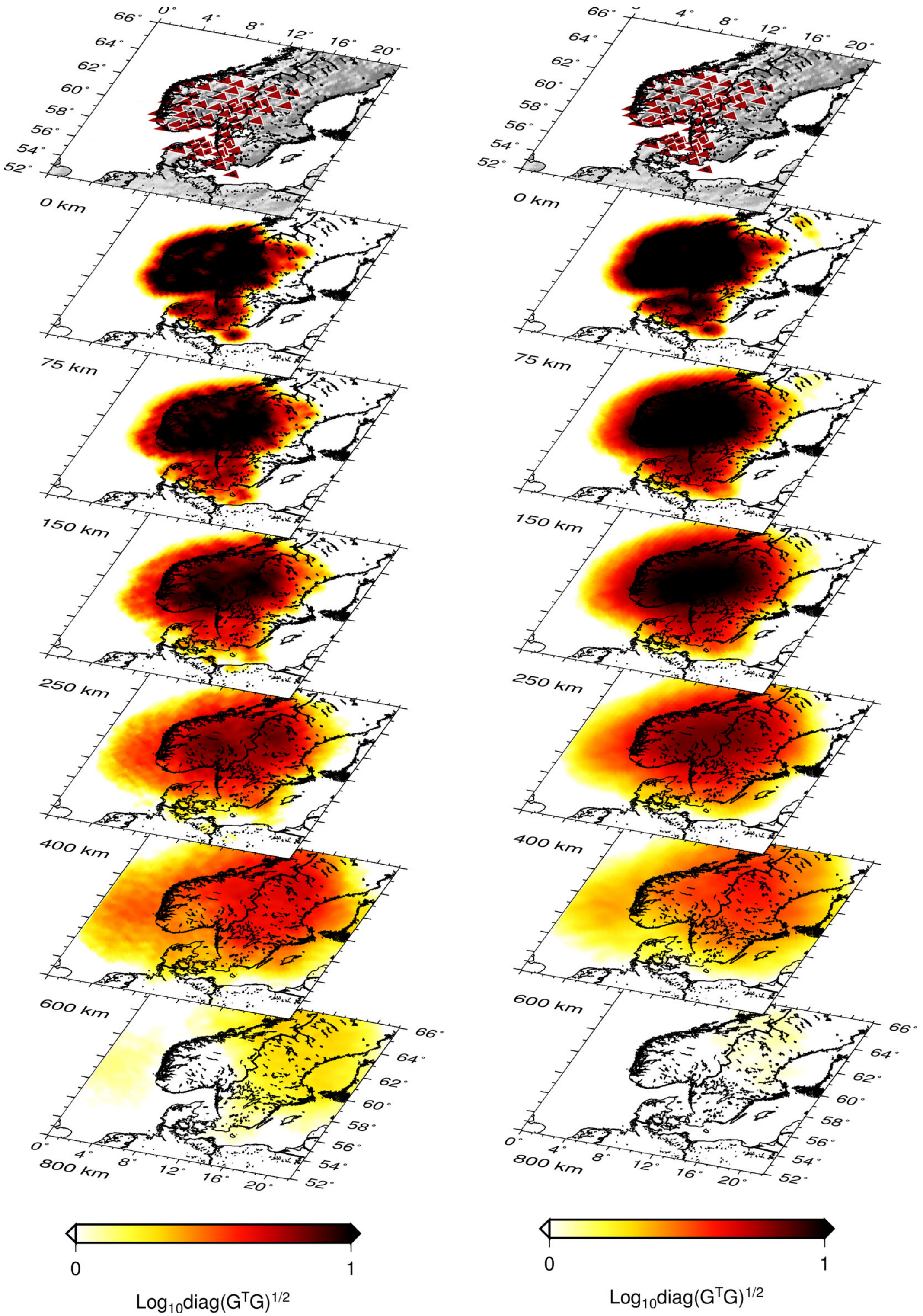

Figure 8. Images of the square root of the diagonal elements of the matrix G^TG. Left: For the *P*-wave tomography. Right: For the *S*-wave tomography.

The values of $\delta ln(V_P/V_S)$ reflect the covariation of V_P and V_S and point consistently to high values of V_P/V_S under southern Norway and low values below Sweden down to a depth of 500 km (Fig. 9). The difference is about 3 per cent between east and west at 150–200 km depth, and even larger in the shallowest part of the mantle.

All anomalies in V_P and V_S, except for the circular low-velocity anomaly in the middle of the study area, have smaller magnitudes below depths of 200 km. Whether this is due to strong heterogeneity in the lithospheric mantle and/or loss of resolution at greater depths is an important question to answer to properly interpret the results. It is also interesting to investigate if the circular low-velocity anomaly could be connected to the deeper mantle but appear disconnected due to decreased resolution at depth, and to estimate the amount of vertical smearing upwards from such a deep anomaly. Equally

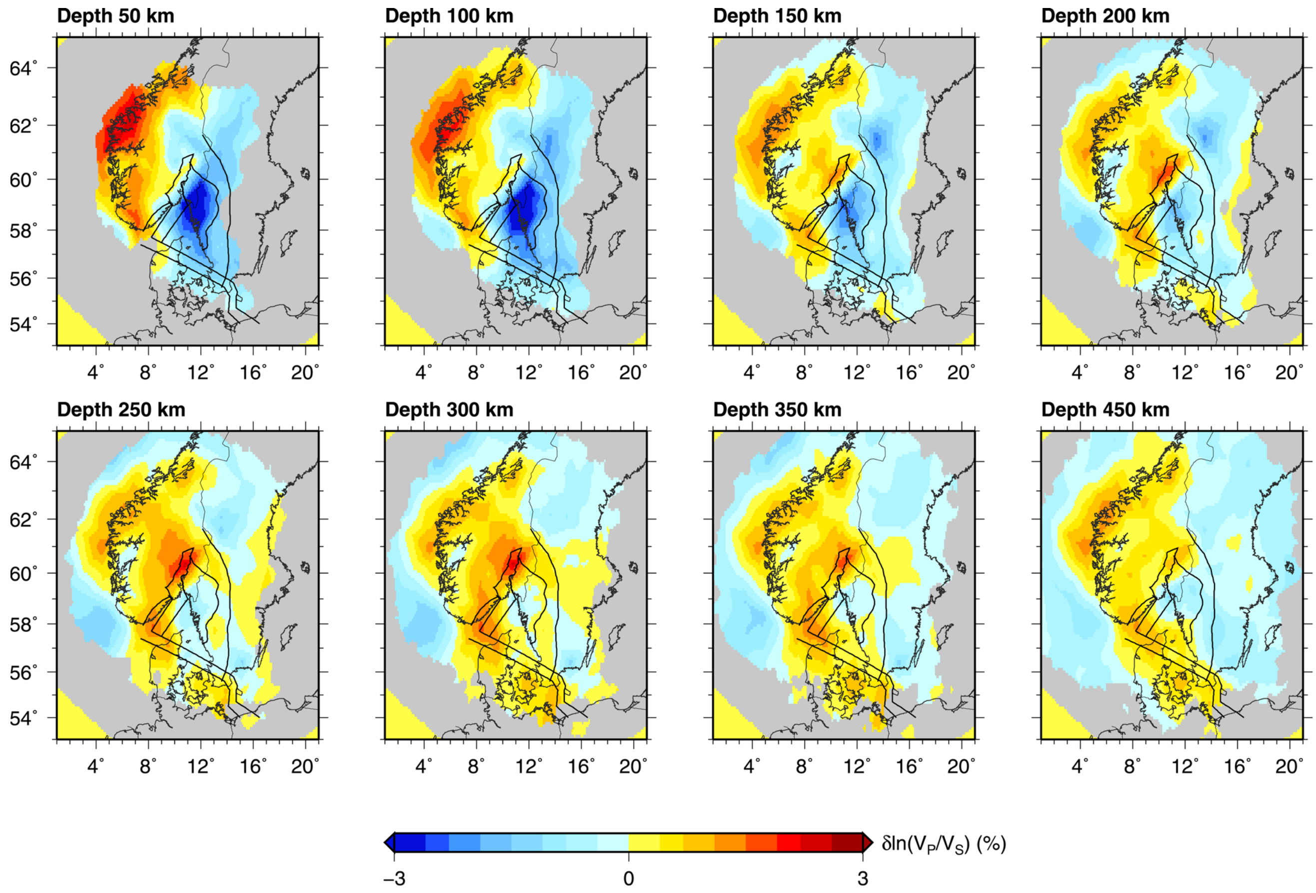

Figure 9. The same as Figs 4 and 5 for $\delta ln(V_\mathrm{P}/V_\mathrm{S})$.

important is the quantification of horizontal smearing between separate anomalies in the uppermost mantle, before we interpret the channel-like low-velocity region as a hot finger reaching out from Norway to Denmark, especially as the data coverage is best in the east-west direction. As we calculate anomalies in the $V_\mathrm{P}/V_\mathrm{S}$ ratio it is also important to quantify uncertainties in $\delta ln(V_\mathrm{P}/V_\mathrm{S})$. Before going to a more detailed interpretation of the models in Section 5, we will investigate their robustness in Sections 4.2–4.4

4.2 Vertical multiscale versus vertical convolutional quelling

The inverted multiscale model is built from synthesizing the largest scale-level first, and hence there is a risk that the resulting structure will be vertically smoothed if the incoming waves are steeply incident with few ray crossings at greater depths. In our data set, epicentral distances are greater than 70° for most events and this might increase the risk of vertical smearing from the multiscale parametrization.

The degree of vertical smearing can be tested by switching off the multiscale parametrization in the vertical direction and use instead convolutional quelling (Meyerholtz *et al.* 1989; Chiao *et al.* 2010) for vertical regularization. Convolutional quelling penalizes model roughness by assigning an *a priori* correlation length to the model (Hung *et al.* 2004; Chiao *et al.* 2010).

We therefore invert for subsurface structure using both the full 3-D multiscale parametrization (hereafter called multiscale) and using a hybrid parametrization with multiscale in the horizontal directions and convolutional quelling with a correlation length of 25 km in the vertical direction (hereafter called hybrid).

Fig. 10 shows tradeoff curves comparing the multiscale and the hybrid schemes for models inverted using the same range of damping values. Model variance, defined as in Chiao *et al.* (2006), is a measure of model uncertainty resulting from data error. This quantity is more appropriate than the usual model norm to calculate L-curves in tomographies with wavelet parametrization, where focus is not on damping the small scales but removing the non-constrained features. It is therefore the model variance which is shown as a function of data misfit, calculated as the squared difference between observed and predicted data normalized by the sum of the squares of the observed data.

Preferred models are chosen near the point of maximum curvature and shown with solid symbols in Fig. 10. The difference between models with damping values around the point of maximum curvature is quite small, with higher damping values suppressing the amplitudes of resulting anomalies slightly. As we perform both *P*- and *S*-wave tomographies, we also perform tests like in Chou *et al.* (2009) to find optimal damping values not only for δlnV_P and δlnV_S separately but also for $\delta ln(V_\mathrm{P}/V_\mathrm{S})$. In these tests we calculate synthetic data for a range of synthetic models with similar magnitude for δlnV_P and δlnV_S (Section 4.4). Hence, the anomalies in $V_\mathrm{P}/V_\mathrm{S}$ should be zero and we search for the damping values giving the smallest artificial anomalies in $V_\mathrm{P}/V_\mathrm{S}$. The chosen damping values in Fig. 10 represent a compromise between model variance, data misfit and stability of the perturbations in $\delta ln(V_\mathrm{P}/V_\mathrm{S})$.

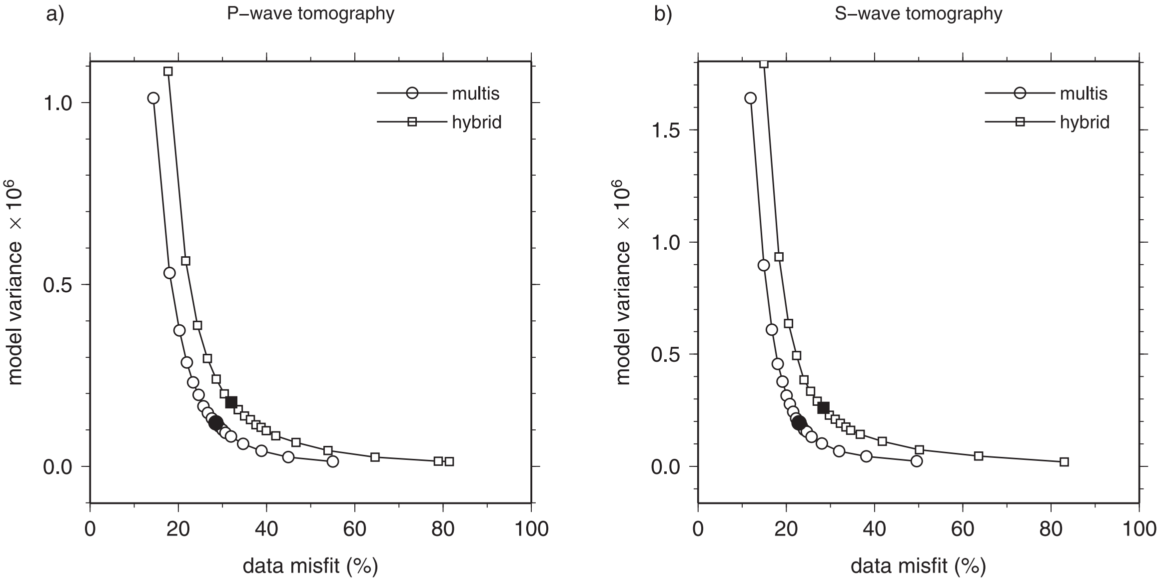

Figure 10. Trade-off between model variance and data misfit for the 3-D multiscale parametrization and the hybrid parametrization with vertical convolutional quelling. (a) *P*-wave models. (b) *S*-wave models. Solid symbols denote the preferred solutions that are shown in Figs 4–7 (multiscale) and Figs 11–12 (hybrid).

The full multiscale inversion clearly has a higher data fit than the hybrid scheme and is the best inversion scheme in that sense. To compare the models derived from the two parametrizations we present in Figs 11 and 12 map views of the hybrid solutions for *P* and *S*, corresponding to the multiscale map views in Figs 4 and 5. The greatest difference between the models is that the multiscale ones have larger anomalies and more small-scale perturbations than the smooth-looking hybrid models.

A wide range of resolution tests of the hybrid and multiscale schemes, whereof some are presented in Section 4.4, show that the full multiscale inversion is better at recovering the amplitude and location of the anomalies. Overdamped multiscale inversions are very similar to underdamped hybrid inversions, and damping values can be chosen such that the results are close to be indistinguishable. As smoothing regularizations are very common, smooth images are typically preferred over more rough pictures of the subsurface by geophysicists, either consciously or unconsciously. The hybrid scheme produces the more smooth and typical tomographic pictures, but all resolution tests (Section 4.4), as well as the data misfit, point out the 3-D multiscale as the superior parametrization. Hence, our preferred model is the one obtained with the full 3-D multiscale inversion. When testing our results in Section 4.4 we pay special attention to vertical resolution and perform all tests using both parametrizations.

4.3 Influence of crustal traveltime corrections

The vertical smearing is most severe in the uppermost parts where the overlap between kernels is smallest, making the influence of crustal corrections quite important. Fig. 13 shows *P*-wave velocities in the uppermost layers inverted from the data set without crustal corrections (Kolstrup 2015), and Fig. 14 shows the corresponding velocities inverted from the corrected data set. The models are grossly similar, but the corrected images have significantly weaker low-velocity anomalies below southern Norway and Denmark in the depths from 0 to 150 km and stronger high-velocity anomalies in the eastern part of the study area. Similar conclusions are drawn for the *S*-wave models (Supporting Information Figs S4 and S5).

The increased magnitude of the channel-like low-velocity region in the uncorrected tomography (Fig. 13) is due to the crust in southern Norway being thicker inland than at the coast, and due to the much thicker sedimentary layers in Denmark compared to the rest of the study area. This gives positive (late) crustal traveltime corrections in central southern Norway and Denmark. In addition, the thinner crust at the Norwegian coast gives negative (early) traveltime corrections that, when not corrected for, result in an overestimation of the high velocities off coast southern Norway. These effects combine to give the expression of a more narrow low-velocity channel with greater magnitude of associated anomalies than in our corrected images (Fig. 14).

It is important to note that the ray-theoretical crustal corrections applied here are not entirely consistent with the finite-frequency measurements, as crustal reverberations have a significant frequency-dependent effect on absolute traveltimes derived with waveform cross-correlation methods (Obayashi *et al.* 2004; Yang & Shen 2006; Ritsema *et al.* 2009). Frequency-dependent crustal corrections (Obayashi *et al.* 2004; Yang & Shen 2006; Ritsema *et al.* 2009) have heretofore been based on the reflectivity method that does not take into account 2-D and 3-D effects (Yang & Shen 2006), making them difficult to apply in a region with a high level of 3-D variation. Recent work shows that, compared to reflectivity-based corrections, ray-theoretical corrections in general overestimate the influence of sedimentary layers and of a thin crust (<30 km) on arrival times measured in the lowest frequency bands (Maupin & Kolstrup 2015, in revision). In our case, ray-theory and reflectivity-based corrections do not differ by more than 0.05 s in Norway and Sweden, but differ by up to 0.6 s for the low-frequency *P*-wave band and for both *S*-wave bands in Denmark due to the overestimation by ray-theory of the influence of the sedimentary layers. The ray-theoretical corrections can therefore be viewed as a maximum bound on the crustal corrections, and the true model in the southwestern part therefore lies somewhere between the ray-theoretically corrected model (Fig. 14), and the model with no corrections (Fig. 13) in the upper 150 km. Similarly for the *S*-wave model (Supporting Information Figs S4 and S5).

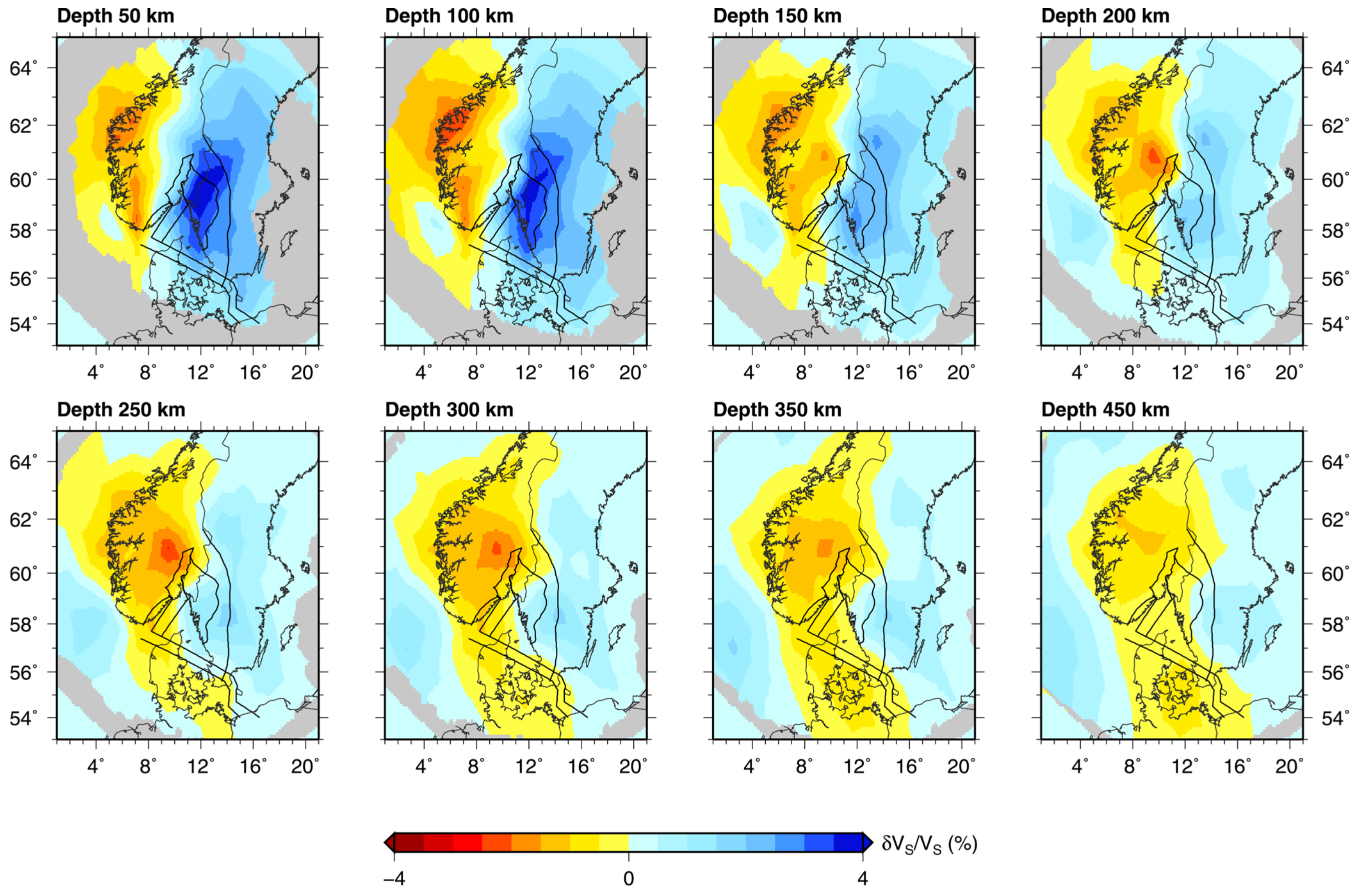

Figure 11. The same as Fig. 4 using the hybrid parametrization.

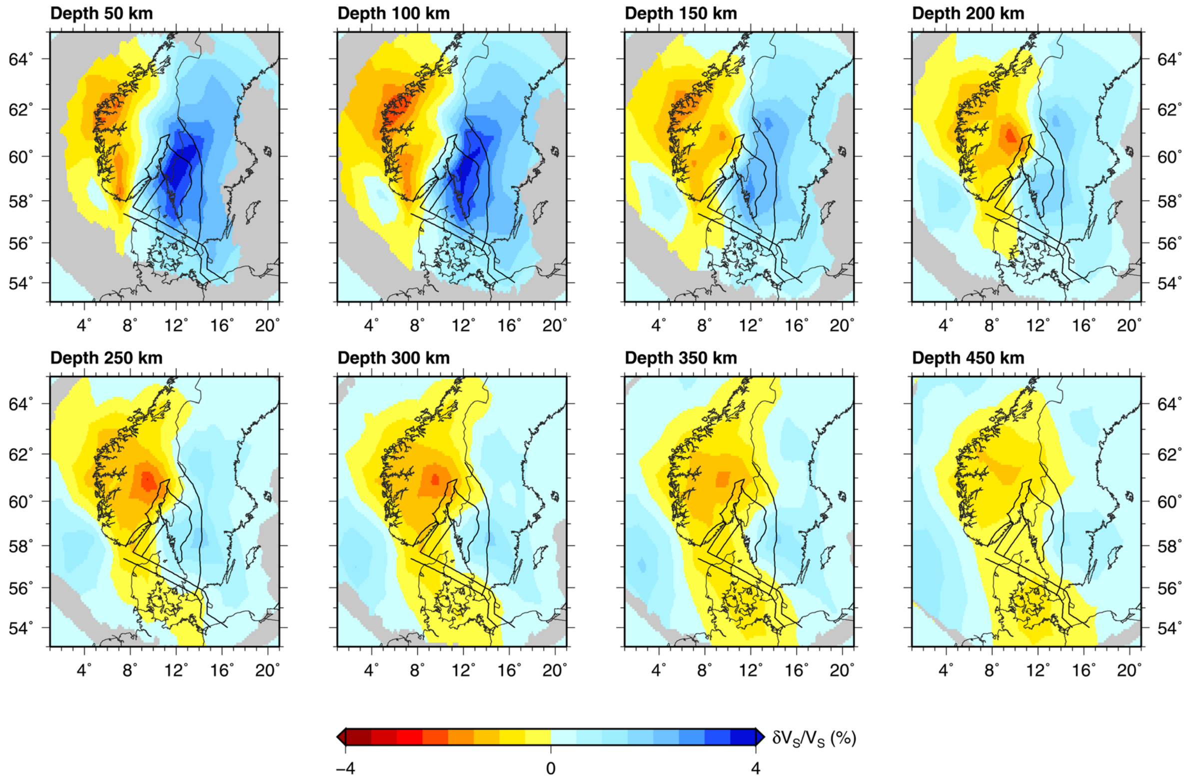

Figure 12. The same as Fig. 5 using the hybrid parametrization.

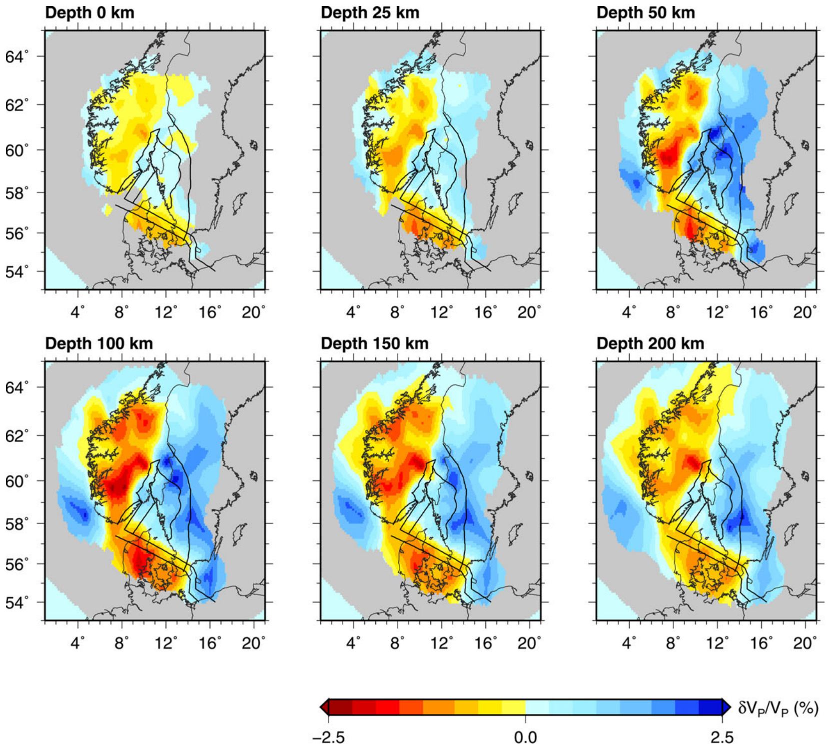

Figure 13. Images of δlnV_P in the uppermost layers. Input data are the raw traveltime residuals without the crustal and topographic corrections from Kolstrup (2015).

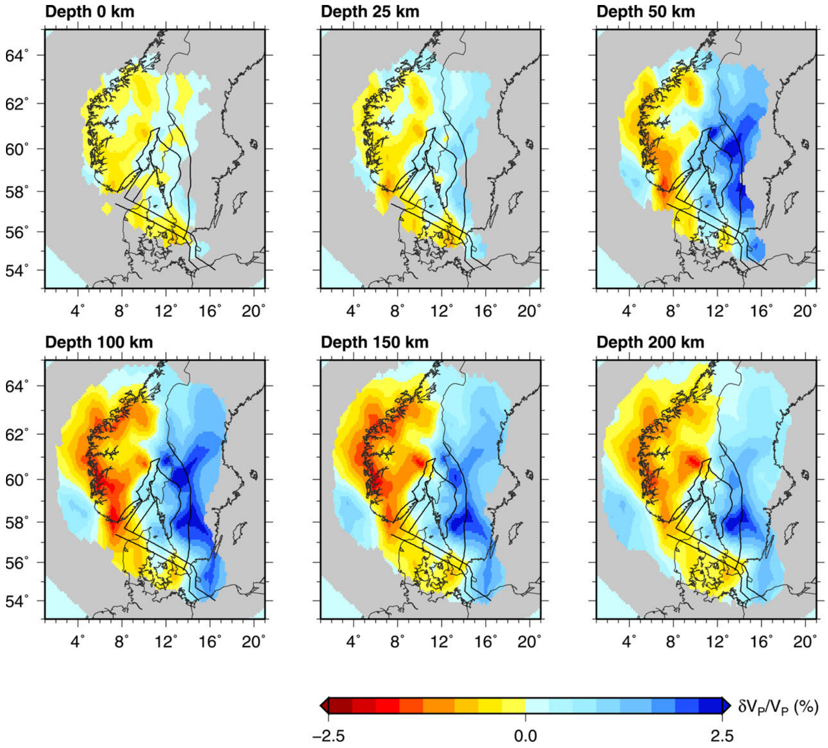

Figure 14. As Fig. 13 but with input data corrected for topography and crustal structure.

Our results show that a robust estimate of the crustal corrections below each station is important to avoid artefacts in the upper 150 km in the tomographic images. In addition, it is important not to lock the crust during inversion, such that the crustal layers can allow for additional perturbations (Martin *et al.* 2005). We also add station and event correction terms in the inversion but assign them a quite low weight, giving them little influence on the results.

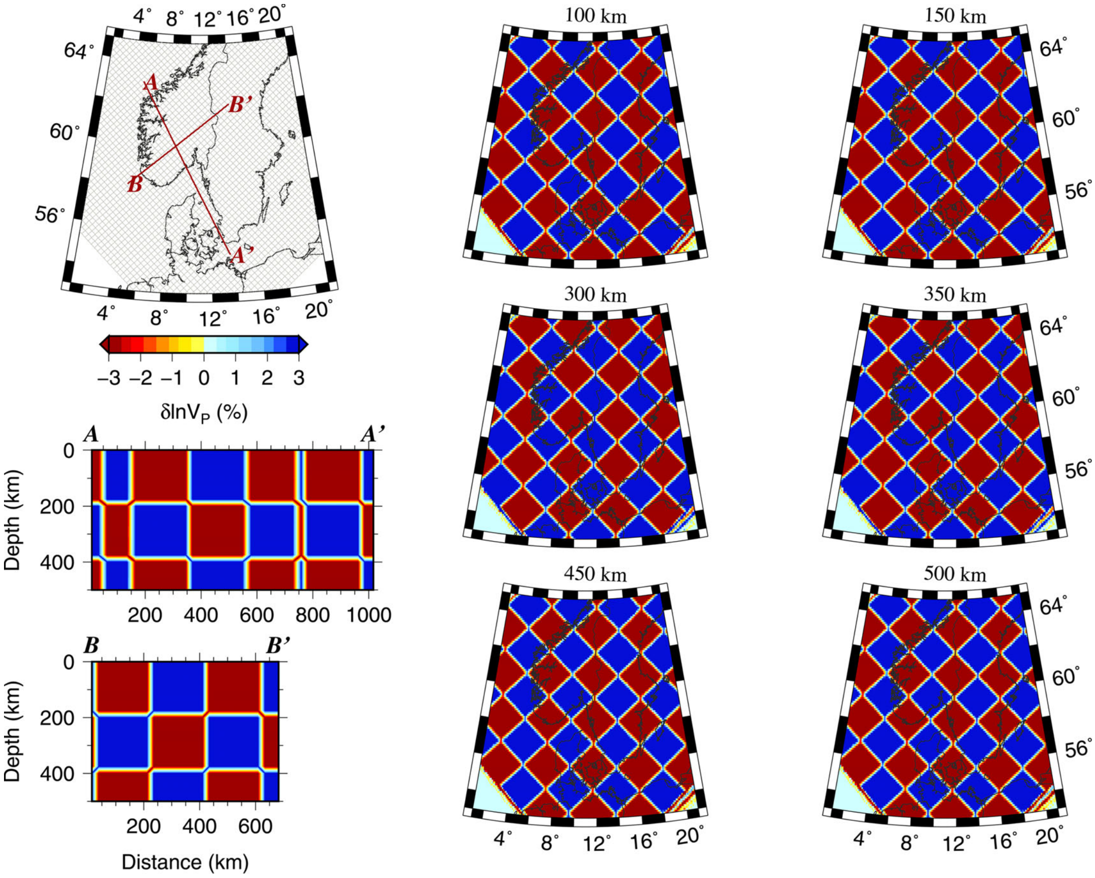

Figure 15. Synthetic input for a chequerboard test with squares of size 200 × 200 × 200 km^3, $\delta lnV_P = \pm 3$ per cent, and $\delta lnV_S = \pm 3$ or ±5 per cent. Upper left map shows location of profiles and grid discretization. The apparent lateral variation of the box size in the profiles is due to the obliquity of the profiles with respect to the chequerboard pattern.

4.4 Resolution tests

We calculate synthetic traveltime data using the *G* matrices built from the actual *P*- and *S*-wave data sets with 3-D finite-frequency kernels, hence using exactly the same source–receiver configuration as in the real tomographies. Random errors with a mean amplitude of about 5 per cent of the average size of the synthetic data is added prior to inversion.

For each synthetic model we test velocity perturbations of 3 per cent in V_P, and both 3 and 5 per cent in V_S. Equal anomalies in V_P and V_S of 3 per cent are used to determine the damping values that give the smallest fluctuations in the $\delta ln(V_P/V_S)$ as in Chou *et al.* (2009).

4.4.1 Horizontal and vertical resolution

We use a range of classical chequerboard tests to estimate the size of objects that can be resolved horizontally and vertically. The starting point is chequerboards of size 200 × 200 × 200 km^3, and Fig. 15 shows the synthetic input for V_P. The full 3-D multiscale inversion results for *P* and *S* waves are shown in Figs 16 and 17, and the corresponding hybrid results for *P* waves are shown in Fig. 18.

It is obvious from Figs 16 and 18 that both the hybrid and multiscale parametrizations recover the input model quite well, but the full multiscale inversion is significantly better at recovering the amplitude and location of anomalies. This result is consistent for all resolution tests, and we show only results for the 3-D multiscale after this first example.

Comparing *P*- and *S*-wave results (Figs 16 and 17), we see that the *P*-wave tomography has better resolution, especially below 200 km depth, but objects of size 200 × 200 × 200 km^3 are quite well resolved in both tomographies. It is also seen that the *S*-wave tomography has more damped anomalies at depth than the *P*-wave tomography. The apparent loss of amplitude in the *S*-wave tomography below depths of 200 km (Fig. 5) might therefore be partly due to loss of resolution at this depth.

Chequerboard tests were also performed using squares of 150 × 150 × 150 km^3 and 100 × 100 × 100 km^3, and with rectangular boxes where the horizontal or vertical length scale was kept constant at 200 km in order to investigate the horizontal and vertical resolution separately. Boxes of size 100 × 100 × 200 km^3 could be well resolved in the *P*-wave tomography, also below 250 km depth. For *S* waves, the horizontal limit of resolution was found to be about 150 km, best in the upper part of the model. Keeping the horizontal length scale constant at 200 km, we found that the limit of vertical resolution was about 150 km in the upper part of the model and 200 km in the lower part, again with the *P*-wave tomography having the best resolution. Hence, we can resolve features with a horizontal scale of about 100 (150) km quite well in the *P*(*S*)-wave tomography, but vertical resolution is limited to about 150–200 km.

The limits of resolution inferred from the chequerboard tests are well below the main features of the models in Figs 4–7. The

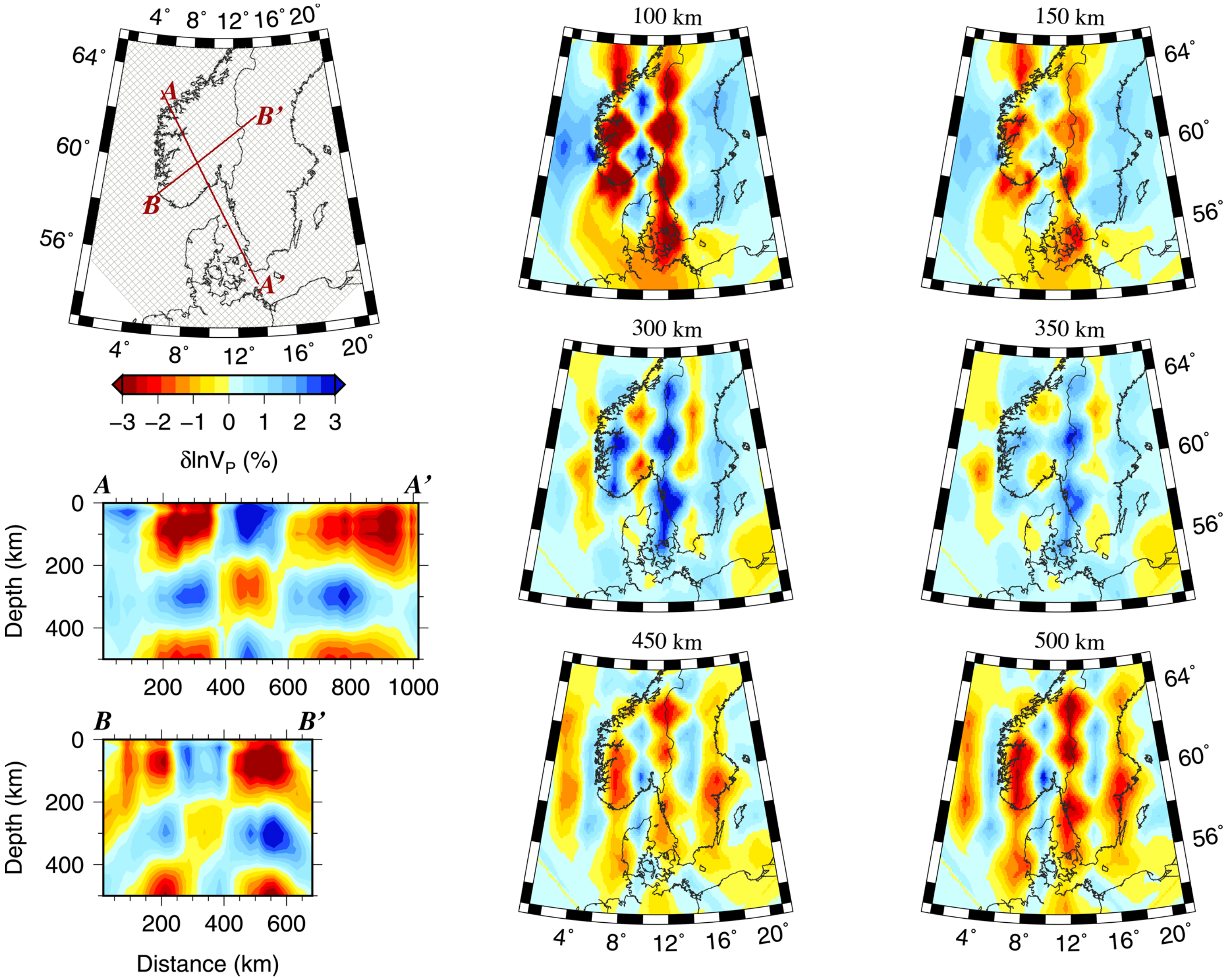

Figure 16. Recovered *P*-wave model using the 3-D multiscale parametrization for the chequerboard test shown in Fig. 15 and synthetic velocity perturbations $\delta lnV_\mathrm{P} = \pm 3$ per cent. Upper left map shows location of profiles and grid discretization.

channel-like low-velocity region is on its thinnest around 150 km wide, though, and the deep cylindrical low-velocity anomaly is quite narrow. In addition, the chequerboard tests created in all cases strong artificial anomalies in the $V_\mathrm{P}/V_\mathrm{S}$ ratio. We analyse therefore in the following sections some synthetic models that simulate naturally occurring anomalies to a larger degree.

4.4.2 The low-velocity channel extending from Norway and Denmark

Regional tomographies on a scale larger than ours (Weidle & Maupin 2008; Rickers *et al.* 2013) show a low-velocity channel from Iceland to southern Norway and Denmark at shallow depths. The ray-theoretical *S*-wave tomography of Wawerzinek *et al.* (2013) shows this channel-like feature at depths of 250–410 km, and the *P*-wave tomography of Medhus *et al.* (2012) shows a tendency of a channel at depths of 100–300 km, but much more blurred than in our images. As the channel imaged in this study might be part of a larger regional feature with geodynamic implications (Weidle & Maupin 2008; Rickers *et al.* 2013), it is important to ascertain whether the channel could result from horizontal smearing of separate anomalies in the uppermost mantle below Norway and Denmark. We place therefore two cylinders extending from 100 to 200 km depths with $\delta lnV_\mathrm{P} = -3$ per cent and $\delta lnV_\mathrm{S} = -3$ or -5 per cent. The cylinder below Norway has a diametre of 180 km and the cylinder below Denmark a diametre of 150 km. From the chequerboard tests we know that anomalies of this size are on the lower limit of resolution, and hence the risk of smearing the synthetic input is large.

The synthetic *P*-wave model is shown in Fig. 19 and the multiscale inversions for δlnV_P and δlnV_S are displayed in Figs 20 and 21. The inversion clearly separates the two cylindrical anomalies and does not smear them into a channel. This indicates that the channel-like feature is indeed a channel and does not represent smearing of separated anomalies in the shallow mantle. The hybrid inversions (not shown) have weaker amplitudes and give a more channel-like appearance of the recovered anomalies.

Using equal δlnV_P and δlnV_S of -3 per cent shows that damping values around 10 000 for both *P* and *S* give the least amount of artificial fluctuations in $\delta ln(V_\mathrm{P}/V_\mathrm{S})$, with $\delta ln(V_\mathrm{P}/V_\mathrm{S})$ being close to zero. These damping values are also reasonable with respect to the trade-off between model variance and data misfit (Fig. 10).

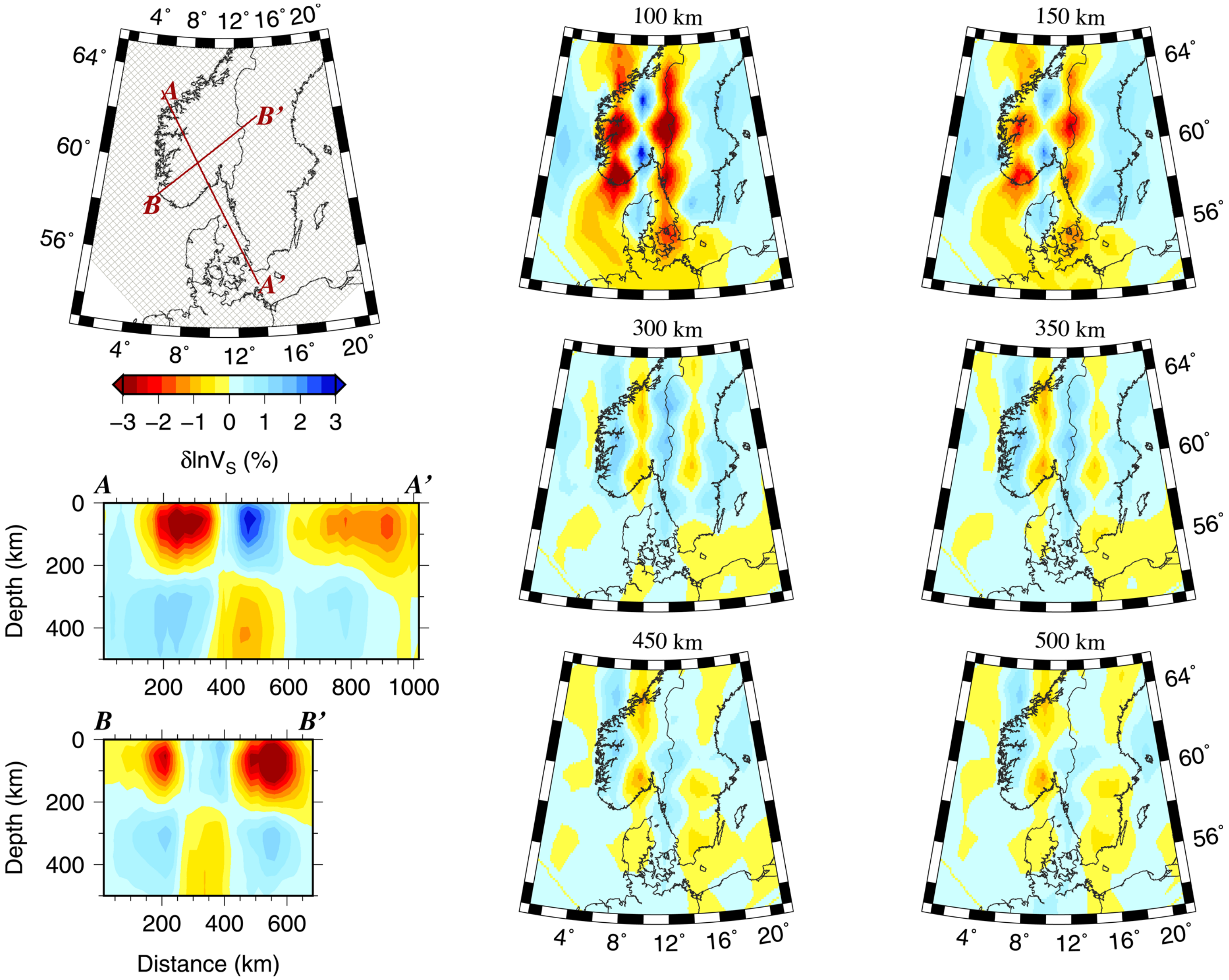

Figure 17. Recovered *S*-wave model using the 3-D multiscale parametrization for the chequerboard test shown in Fig. 15 and synthetic velocity perturbations $\delta ln V_S = \pm 3$ per cent. Upper left map shows location of profiles and grid discretization.

Fig. 22 shows the resulting $\delta ln(V_P/V_S)$ for a synthetic input of +2 per cent ($\delta ln V_P = -3$ per cent and $\delta ln V_S = -5$ per cent). The recovered $\delta ln(V_P/V_S)$ is below 1 per cent and much smaller than the anomalies in the real tomography (Fig. 9), implying that the real anomalies have a larger contrast in V_P/V_S, or that they are better recovered than the small synthetic objects.

The vertical smearing of $\delta ln(V_P/V_S)$ is also much more severe than for V_P and V_S separately, due to the larger degree of vertical smearing of the *S*-wave tomography and the combined uncertainties of the *P*- and *S*-wave data sets. This test, along with the chequerboard tests, shows that we cannot interpret depth variations of the V_P/V_S ratio, but that we have robust estimates of horizontal variations averaged over depth. Hence, we can interpret the strong west to east variation in $\delta ln(V_P/V_S)$ in Fig. 9.

4.4.3 The deep cylindrical low-velocity anomaly below central southern Norway

The cylindrical low-velocity anomaly in the centre of the study area extends from depths of approximately 150–350 km (Figs 4 and 5). As the resolution decreases at greater depths, we test if a cylinder located from 150 to 500 km depth gives a similar image as a cylinder confined to depths of 150–350 km. The synthetic cylinder has a diametre of 100 km and a velocity perturbation of $\delta ln V_P = -3$ per cent and $\delta ln V_S = -3$ per cent or −5 per cent.

The synthetic input model is shown in Fig. 23 and the inverted *P*-wave model is shown in Fig. 24. Obviously, the *P*-wave anomaly is recovered down to depths of around 450–500 km. The results for a similar cylinder extending only to a depth of 350 km (not shown) are much more similar to the anomaly found in the tomographic images in Figs 4 and 5. Similar tests were also performed using broader cylinders with diametres of 120 and 150 km, giving similar results but much stronger recovered anomalies. Hence, we can be quite confident that the cylindrical low-velocity anomaly does not extend below 350–400 km depth and that it is indeed quite narrow with a diametre of about 100 km.

We also tested if the cylindrical low-velocity anomaly could result from vertical smearing of separate anomalies by placing two cylinders at depths from 100 to 200 km and 300 to 400 km. Both cylinders have a diametre of 100 km and velocity perturbations

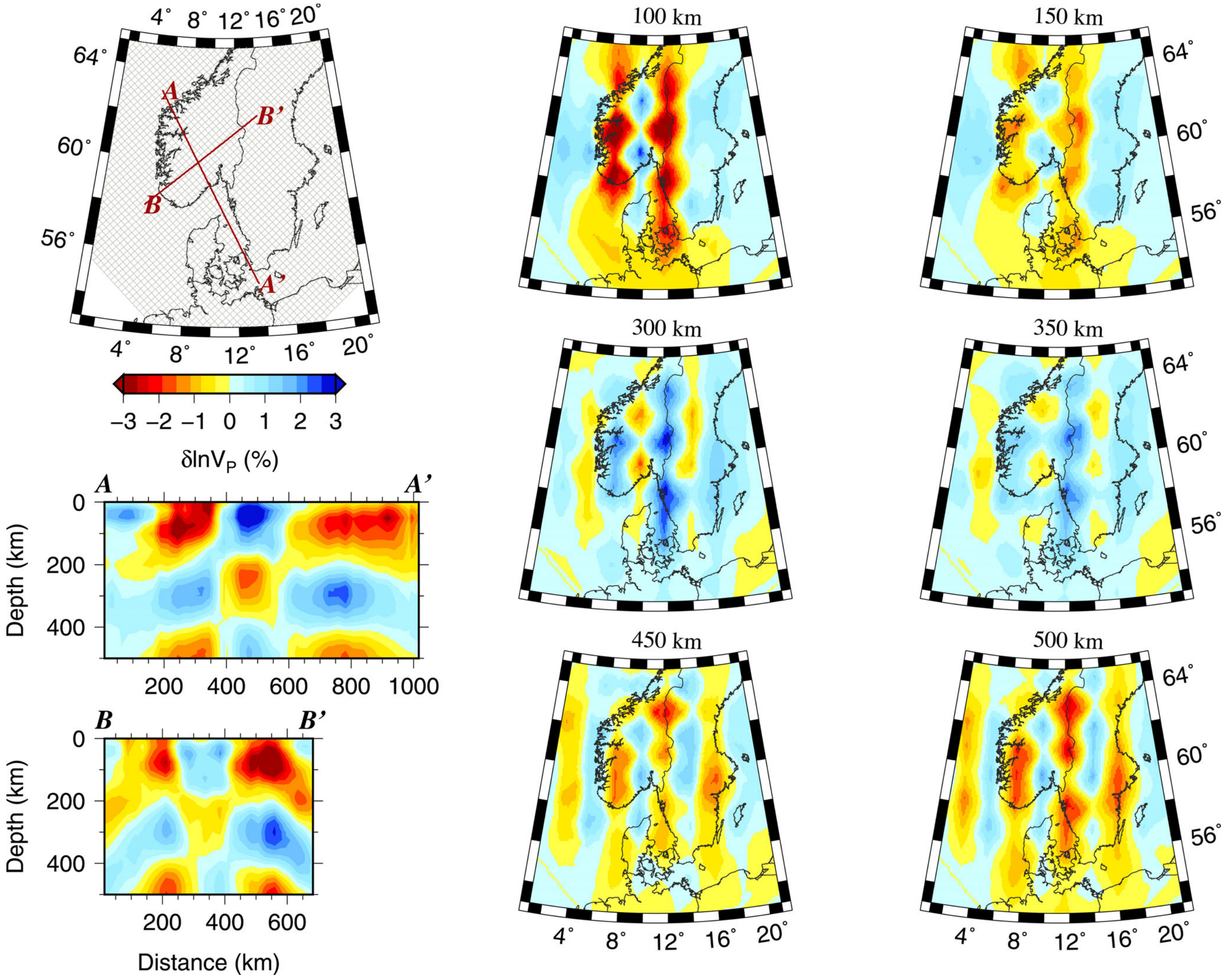

Figure 18. The same as Fig. 16 using the hybrid parametrization.

of $\delta lnV_{\mathrm{P}} = -3$ per cent and $\delta lnV_{\mathrm{S}} = -5$ per cent (Supporting Information Fig. S1). The recovered anomalies (Supporting Information Figs S2 and S3) are smeared into a continuous cylinder, but with much smaller amplitudes than the input anomalies: about −1 per cent in V_{p} and −1.5 per cent in Vs. It is therefore more likely that the strong cylindrical anomaly in the tomography represents a continuous feature than the result of vertical smearing.

4.5 Ray-theoretical multiscale tomographies

As an additional check of our results, we also perform an inversion of the data with a ray-theoretical approach instead of the finite-frequency kernels, facilitating comparison of our results with the recent ray-theoretical tomographies of Medhus *et al.* (2012) for *P* waves and Wawerzinek *et al.* (2013) for *S* waves. These two studies use the same databases as we do, but different methods to measure traveltimes. We invert the high-frequency band of our data sets using the same multiscale parametrization and gridding as in the finite-frequency tomography. Resolution tests were also performed but are not shown.

The resulting δlnV_{P} model is displayed in Fig. 25 and shows more similarity with the relative tomography of Medhus *et al.* (2012) than the finite-frequency model in Fig. 4. The important difference between the ray-theoretical images (Fig. 25) and the finite-frequency images (Fig. 4) is that the inclusion of the low-frequency data increases the sensitivity to velocity anomalies off coast and across the Skagerrak Sea between Norway and Denmark. In our ray-theoretical inversions, we lose the clear image of a channel and only sense the western high-velocity anomaly in a small area close to the southwestern coast of Norway. This is very similar to the relative tomography of Medhus *et al.* (2012), and confirms that the inclusion of low-frequency data increases resolution due to the different spatial sensitivity of finite-frequency measurements in different pass bands.

A ray-theoretical *S*-wave tomography is shown in Fig. 26. Compared to the finite-frequency images in Fig. 5 the ray-theoretical tomography has smaller anomalies and less resolution off coast. The main features of the V_{SH} images in Figs 5 and 26 are similar to the images of Wawerzinek *et al.* (2013) but the amplitudes are much larger. Wawerzinek *et al.* (2013) infer a quite deep low-velocity anomaly down to depths of 410 km where our images confine this deeply going anomaly to depths of around 350 km and to a smaller horizontal area. The increased recovery of amplitudes in our images can be ascribed to both the multiscale parametrization and the finite-frequency kernels.

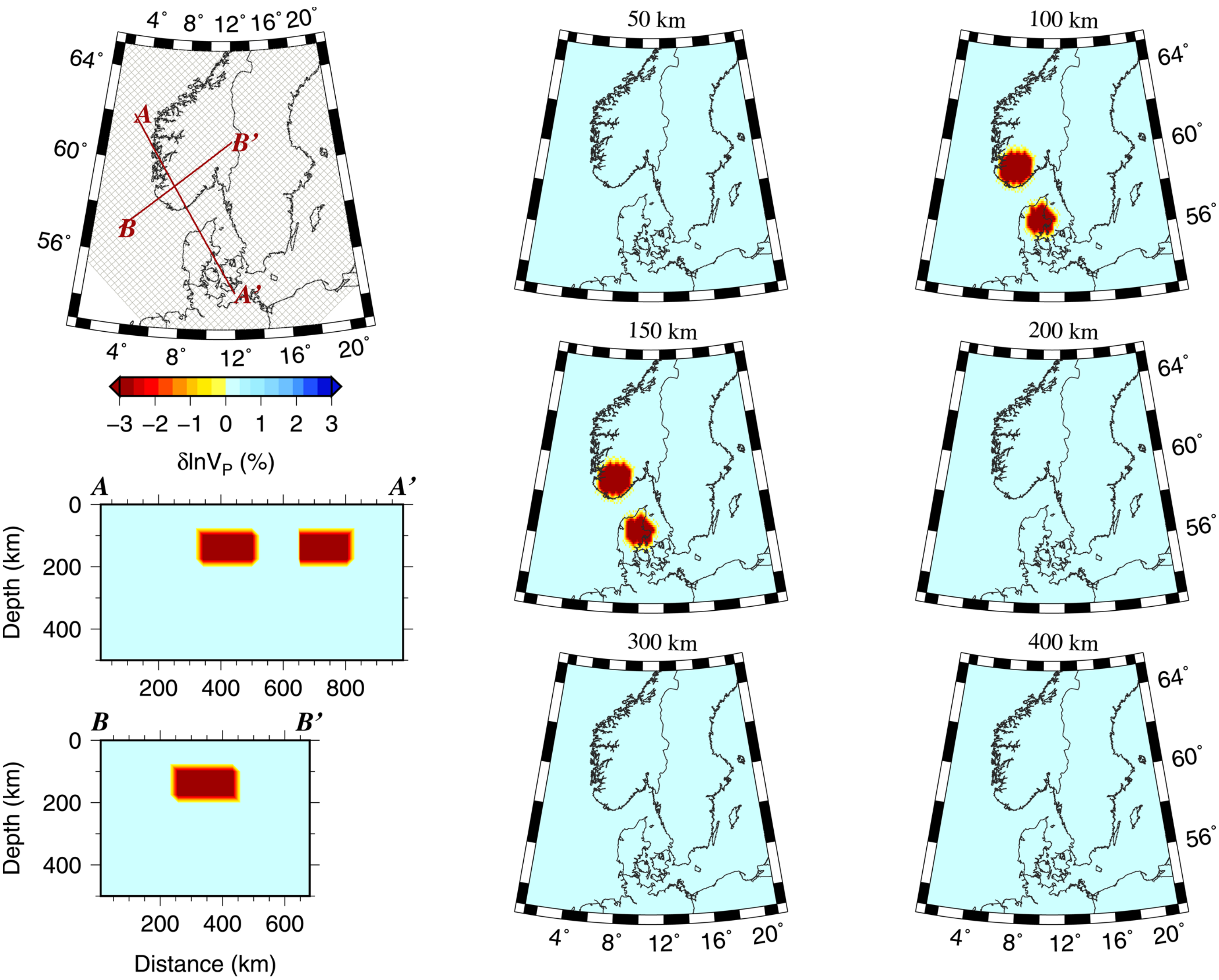

Figure 19. Synthetic input for a test with two cylinders in the depth range from 100 to 200 km and with diametres of 150 and 180 km. The velocity perturbations are $\delta V_{\rm P} = -3$ per cent and $\delta V_{\rm S} = -3$ or -5 per cent. Upper left map shows location of profiles and grid discretization.

5 DISCUSSION

Resolution tests show that we have three main well-resolved features in our models: a low-velocity channel extending from western Norway to Denmark, a deeper cylindrical low-velocity anomaly below central southern Norway, and a belt of high velocities below Sweden. The lateral boundary between the high and low velocities is imaged with great detail in the horizontal directions, and its development with depth is also robustly constrained. For $V_{\rm P}/V_{\rm S}$ ratios, resolution tests show a high degree of vertical smearing, implying that vertical variations are very poorly constrained, but (depth-averaged) lateral variations are robustly constrained down to 250–300 km depth.

5.1 Comparison to previous seismological studies

Our study reproduces the low velocities below southern Norway and Denmark and high velocities of the Fennoscandian Shield found by recent local geophysical investigations (Maupin 2011; Medhus *et al.* 2012; Köhler *et al.* 2012; Wawerzinek *et al.* 2013; Maupin *et al.* 2013) and regional studies of western Europe (Weidle & Maupin 2008; Zhu *et al.* 2012; Fichtner *et al.* 2013; Rickers *et al.* 2013; Zhu *et al.* 2013). Our study adds to this large-scale picture some important details that have not been imaged in previous studies. The low velocities below southern Norway and Denmark consist of two clearly distinct features: a quite narrow channel at shallow depths to the west, and a deeper, cylindrically shaped anomaly centred at the northern end of the Oslo Graben.

On a larger regional scale, Zhu *et al.* (2012, 2013) image a low-velocity channel in $V_{\rm SV}$ and isotropic $V_{\rm S}$ at shallow depths below southern Norway, and quite interestingly, also an inversion of the low velocities at depths below 475 km where a high-velocity anomaly is placed below southern Norway and Denmark. The low velocities below southern Norway are also seen in the regional tomographies of Weidle & Maupin (2008) and Fichtner *et al.* (2013).

Rickers *et al.* (2013) focuses on the North Atlantic region and image a channel with approximately −4 per cent anomaly in $V_{\rm SH}$ (with respect to a European 1-D average model) connecting the Iceland hotspot to southern Norway and Denmark. The low-velocity channel has its maximum between depths of 100–200 km but extends to a depth of 300 km. In the North Sea, northwest of southern Norway, the anomaly increases in strength and depth. This is also

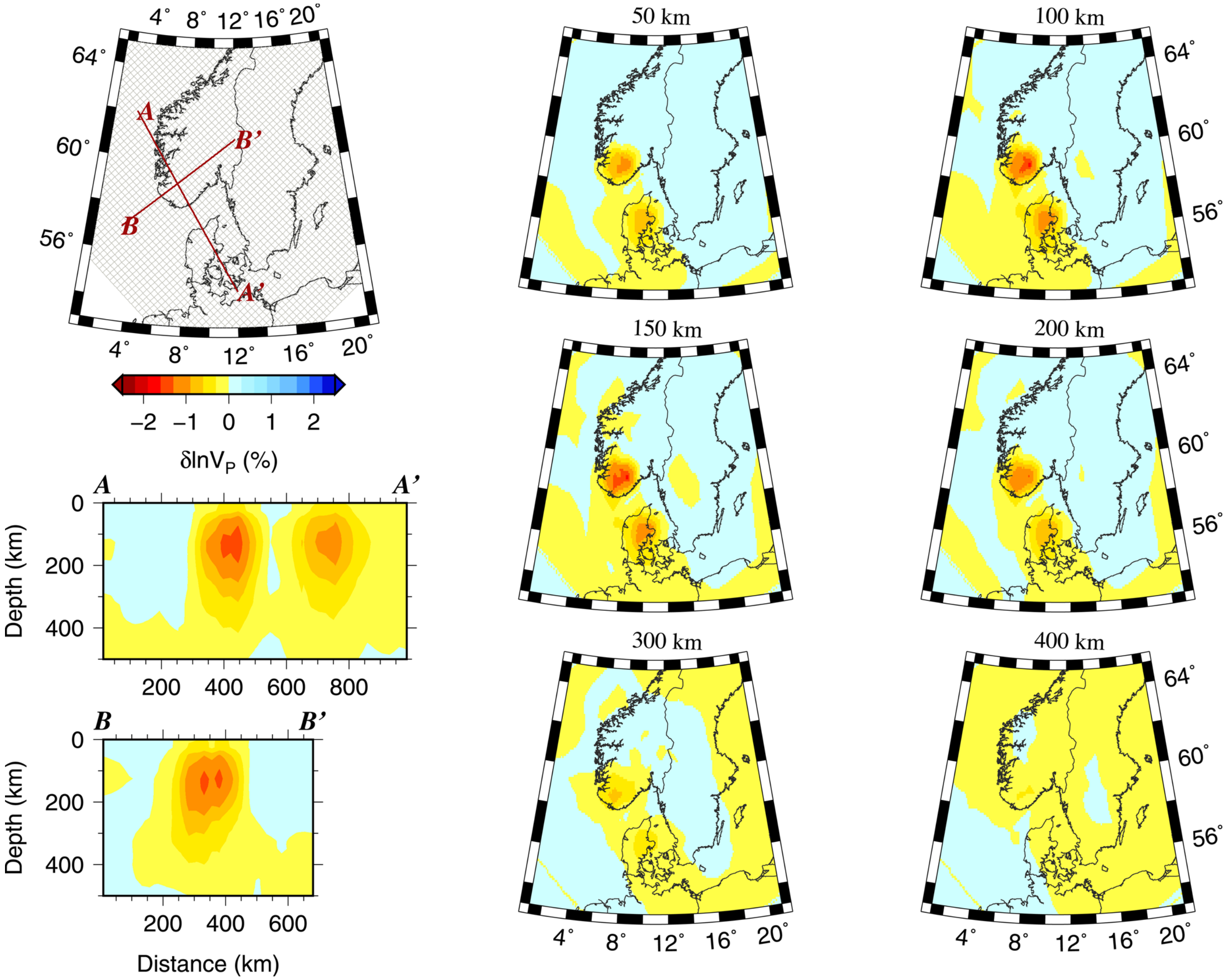

Figure 20. Recovered *P*-wave model using the 3-D multiscale parametrization in a test with the synthetic model shown in Fig. 19 and velocity perturbation $\delta lnV_P = -3$ per cent. Upper left map shows location of profiles and grid discretization.

the region where we infer the lowest velocities, especially in the *S*-wave tomography (Fig. 5). In the Central Graben area, southwest of Norway and Denmark, Rickers *et al.* (2013) find high-velocity anomalies between 2 to 3 per cent, confirming the high velocities off coast southern Norway and Denmark in our images. Although the relative magnitudes of anomalies in our images cannot be compared directly to the absolute velocity anomalies in the tomography of Rickers *et al.* (2013), we find a very similar low-velocity channel in V_{SH}, the only difference being the higher degree of detail in our tomography.

Local studies based on surface waves (Maupin 2011; Köhler *et al.* 2012) also confirm this general picture of low velocities below southern Norway, but on this scale it is even more natural to compare our results with the recent *P*- and *S*-wave tomographies of Medhus *et al.* (2012) and Wawerzinek *et al.* (2013) already mentioned in the previous sections.

Medhus *et al.* (2012) were the first to clearly image the lateral boundary between low and high *P*-wave velocities that continues quite surprisingly from the Tornquist-Teisseyre Zone (TTZ) and Sorgenfrei-Tornquist-Zone (STZ) in northern Germany and Denmark into southern Norway. Our tomographic images show a boundary between low and high velocities in both V_P and V_{SH} that follows the STZ (Fig. 1) to an even larger degree than in the tomographies of Medhus *et al.* (2012) and with a correlation that extends to depths of around 300 km. The greatest difference between our study and the work of Medhus *et al.* (2012) is that we infer high velocities off coast western Denmark and Norway, which confines the low velocities to a shallow channel, instead of a boundary between two half-spaces. In addition, we image much more clearly the presence of a deeper low-velocity structure below the northwestern end of the Oslo Graben, and infer in general higher magnitudes of velocity anomalies.

Where the *P*-wave study of Medhus *et al.* (2012) and *S*-wave study of Wawerzinek *et al.* (2013) estimate velocity anomalies of about equal magnitudes, our study images V_{SH} anomalies with magnitudes about twice the size of the V_P anomalies, as expected from both theoretical calculations (e.g. Goes *et al.* 2000) and seismological models (e.g. Kennett *et al.* 1998). In addition our *P*- and *S*-wave tomographies show much less difference in the spatial distribution of anomalies than the tomographies of Medhus *et al.* (2012) and Wawerzinek *et al.* (2013), showing the importance of regularization and parametrization for seismic models (e.g. Trampert & Snieder

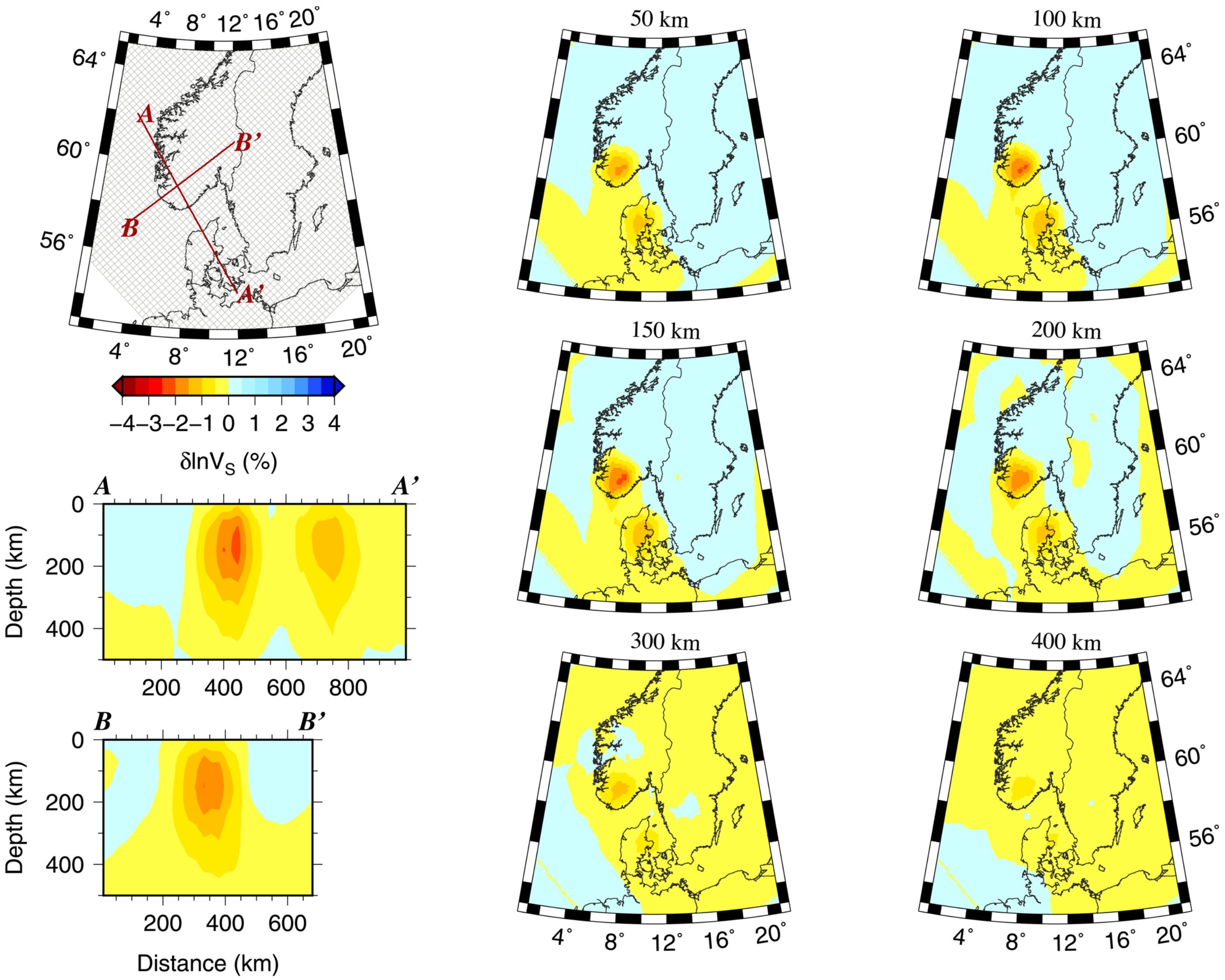

Figure 21. The same as Fig. 20 for $\delta lnV_S = -5$ per cent.

1996; Chiao & Kuo 2001; Nolet 2008; Chiao *et al.* 2010). Estimating robust perturbations of V_P/V_S is therefore only possible when using similar parametrization and regularization of the *P*- and *S*-wave models, or when making joint inversions of the *P*- and *S*-wave data sets.

5.2 Comparison to non-tomographic studies

It seems clear that main structures we image are concordant with previous seismological studies but we recover more realistic magnitudes of the *P*- and *S*-wave anomalies.

It is very interesting to note that the gravity modelling of Ebbing *et al.* (2012) shows a quite strong contribution to surface topography from some non-crustal source, for example the upper mantle, in the location where we image the low-velocity channel, but they do not estimate any contribution to topography where we image the deep circular anomaly. This could mean that the causes of the two low-velocity anomalies are different. Care should be taken that part of this estimated buoyancy from the mantle could be caused by uncertainties in Moho depth, as receiver function studies and active seismics infer different Moho depths, with up to 8 km difference, in the Western Gneiss Region (WGR, Fig. 1) at the northwestern coast of southern Norway (Svenningsen *et al.* 2007; Stratford & Thybo 2011; Frasetto & Thybo 2013; Kolstrup & Maupin 2013).

Another gravity study that estimates a contribution to the surface topography from the mantle is the study of Jones *et al.* (2002). They use the long-wavelength (>750 km) free-air gravity anomaly field to estimate the dynamic contribution to topography and infer a contribution on the order of 500–1000 m in southern Norway. Rickers *et al.* (2013) noted a strong correlation between the low-velocity anomalies in their North Atlantic tomography with both the areas of positive residual topography in Jones *et al.* (2002) and with continental regions estimated to have experienced major Neogene uplift (e.g. Japsen & Chalmers 2000). This suggests that the correlation between the low-velocity anomalies in our images and the mantle contribution to topography in Ebbing *et al.* (2012) is not coincidental.

It is also interesting that the low-velocity channel is associated with a high degree of intraplate seismic activity (e.g. Lindholm *et al.* 2000; Bungum *et al.* 2010) that continues from the North Sea along the coast of western Norway and to northwestern Denmark (Fig. 1). The cause of the seismic activity is not believed to be post-glacial rebound and is more likely caused by a combination of for example ridge push, sedimentation and/or lateral lithospheric differences

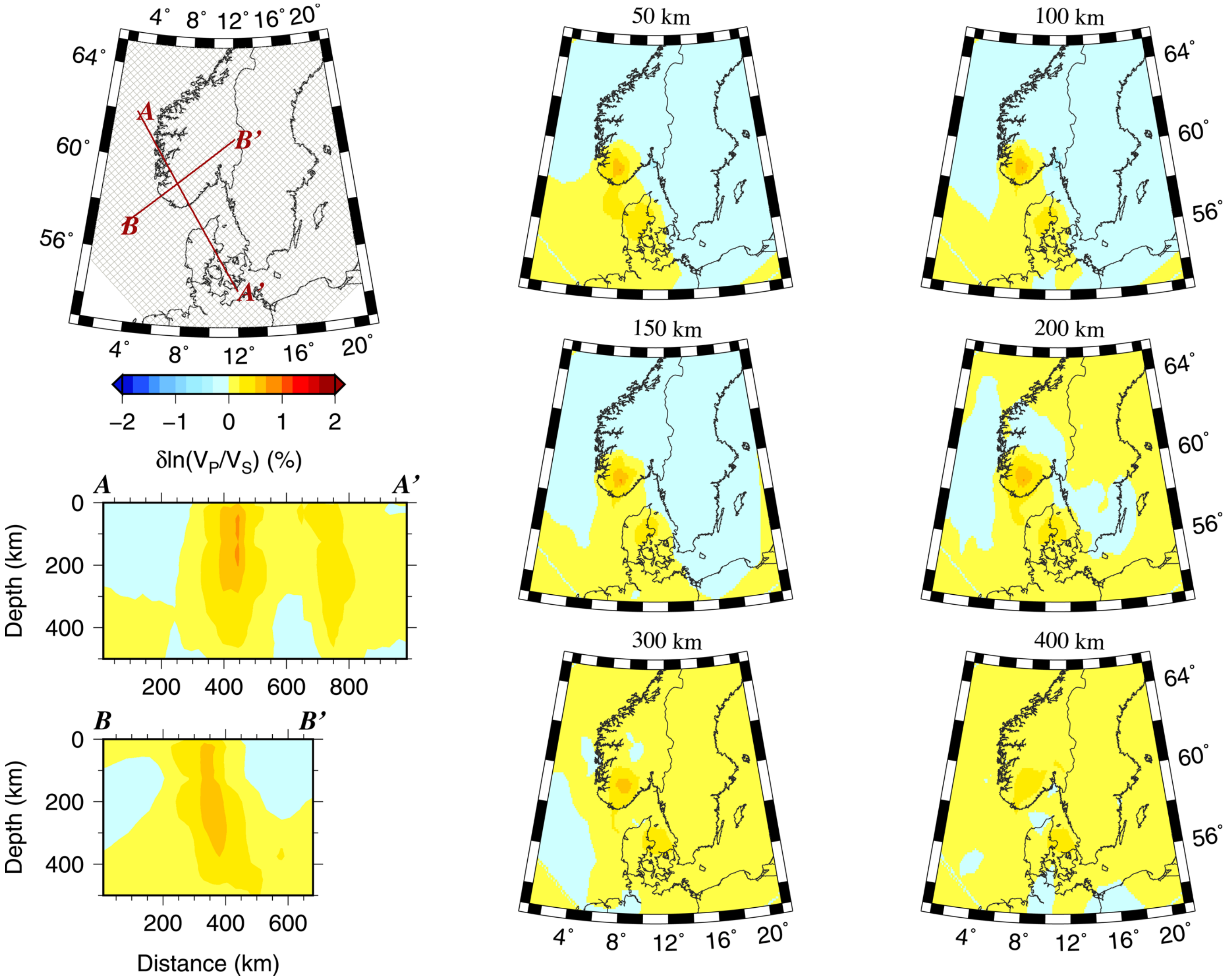

Figure 22. The same as Figs 20 and 21 for $\delta ln(V_P/V_S) = 2$ per cent.

(Bungum *et al.* 2010). A similar concentration of intraplate stresses and seismicity in lithospheric 'thin spots' has been described in the case of SE Brasil (Assumpção *et al.* 2004). Our study clearly images lateral lithospheric differences and suggests that intraplate stresses concentrate in areas with a thinner lithosphere. The narrow and deep cylindrical low-velocity anomaly in the northwestern end of the Oslo Graben is not associated with any centre of seismic activity, and this again suggests that it is different from the more shallow channel-like anomaly.

5.3 Tectonophysical implications—$\delta ln V_P$, $\delta ln V_S$ and temperature variation

If low seismic velocities below the passive margins of the North Atlantic are indeed associated with dynamic support of topography from the mantle and Neogene uplift, as suggested by Rickers *et al.* (2013), it is quite important to quantify the anomalies in terms of temperature and/or composition and investigate their tectonic implications.

Within the upper subcontinental mantle and away from the hydrated regions close to subduction zones, seismic velocity anomalies are best explained by variations in temperature (from either convection, changes in lithospheric thickness and/or changes in heat production) and iron content (from melt extraction or metasomatic refertilization; e.g. Goes *et al.* 2000; Poudjom Djomani *et al.* 2001; Griffin *et al.* 2009). Separating the effects of the two parameters is notoriously difficult (Cammarano *et al.* 2003) and perhaps only possible in extreme cases where Archean and tectonically young lithospheres are compared (Goes *et al.* 2000).

As anhydrous variations in composition give seismic velocity variations smaller than 1–2 per cent in Proterozoic and younger tectonic regions (Goes *et al.* 2000; Cammarano *et al.* 2003; Griffin *et al.* 2009; Hieronymus & Goes 2010), we can make an end-member interpretation of the high- and low-velocity anomalies in terms of temperature. Using for example derivatives of V_S velocity with respect to temperature from the literature ($\partial ln V_S/\partial T \approx -1$ per cent/100 K, Lee 2003), V_S velocity anomalies of ± 3 per cent translate into temperature anomalies about $\mp 300\,^{\circ}$C.

The main problem with this linear interpretation of seismic high- and low-velocity anomalies into hot and cold, is that shear anelasticity makes the temperature derivatives of V_P and V_S strongly temperature-dependent and the absolute value of the derivatives increases with increasing temperature (Cammarano *et al.* 2003). Velocity anomalies of different sign therefore give temperature

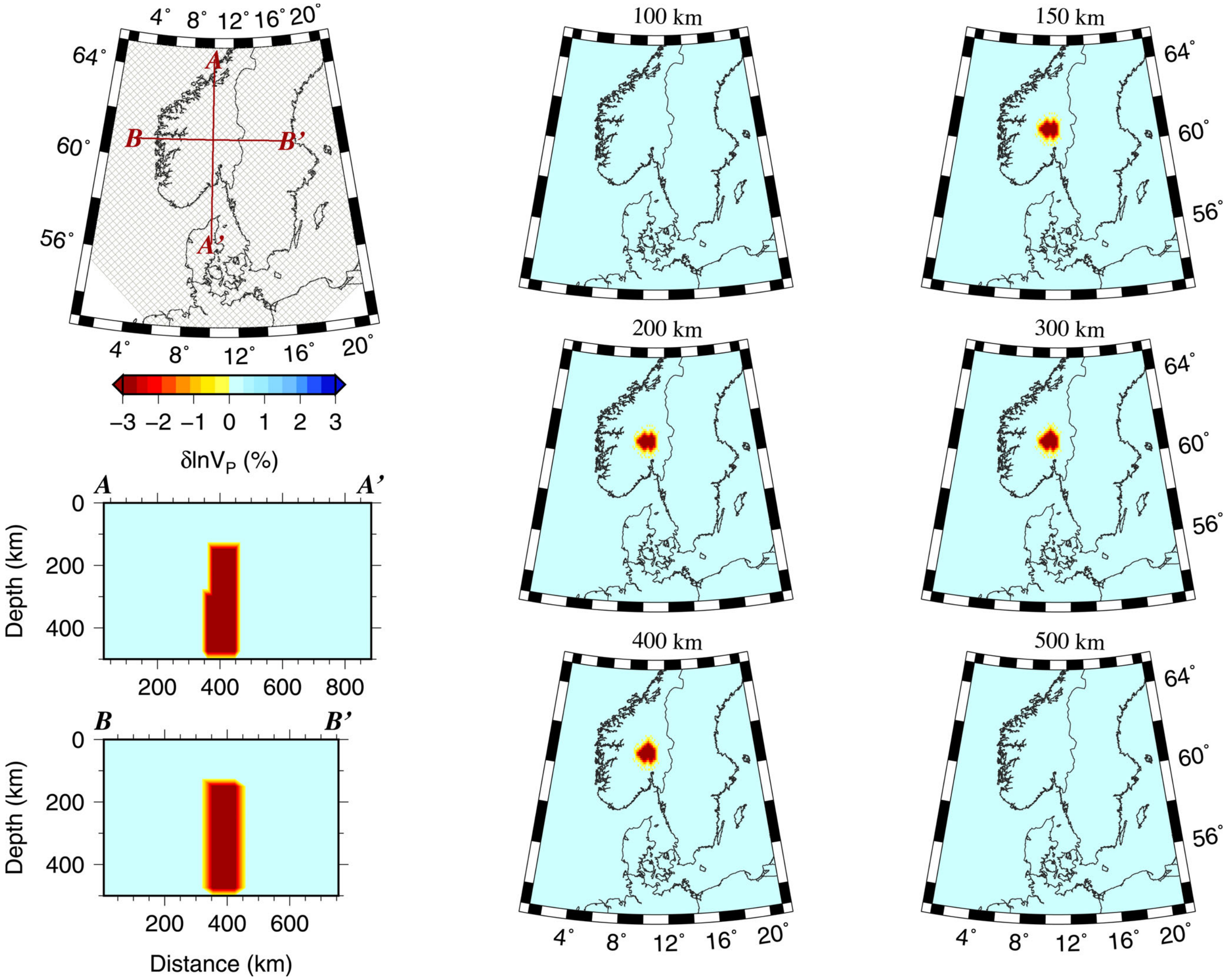

Figure 23. Synthetic input for a test with one cylinder extending from 150 to 500 km depth and with a diametre of 100 km. The velocity perturbations are $\delta lnV_{\mathrm{P}} = -3$ per cent and $\delta lnV_{\mathrm{S}} = -3$ or -5 per cent. Upper left map shows location of profiles and grid discretization.

anomalies of different magnitude, and absolute seismic velocities are needed to make a thermal interpretation (Goes *et al.* 2000; Cammarano *et al.* 2003). In addition, the anelasticity parameters used in calculating velocities and velocity derivatives (e.g. Berckhemer *et al.* 1982; Sobolev *et al.* 1996; Jackson *et al.* 2002; Shapiro & Ritzwoller 2004) also have a significant effect on the magnitude of estimated velocities (e.g. Goes *et al.* 2000; Cammarano *et al.* 2003; Kolstrup *et al.* 2012).

Due to these complications we take a more indirect approach in the interpretation of the velocity anomalies in Figs 4–7 and compare our results to those obtained by thermal lithosphere modelling in the study area (Kolstrup *et al.* 2012; Gradmann *et al.* 2013).

Kolstrup *et al.* (2012) modelled the temperature field and predicted seismic velocities in southern Norway using several geophysical data sets (Moho depth, geoid, surface heat flow), taking into account the dependence of seismic waves on temperature, composition and anelasticity at high temperature and pressure. To limit the range of possible models fitting the data sets, they used a constraint of local isostatic equilibrium for the lithospheric column overlying an adiabatic asthenosphere. Kolstrup *et al.* (2012) inferred a thin and warm lithosphere (∼100 km) in western Norway and a thick and cold lithosphere in eastern Norway and Sweden (∼200 km), and additionally a slightly thinner and warmer area associated with the Oslo Graben. The maximum relative difference in synthetic seismic shear wave velocity between the thin western lithosphere and the thick eastern lithosphere in Kolstrup *et al.* (2012) is up to 8.5 per cent at 100 km depth ($\Delta T \approx 400\,^{\circ}\mathrm{C}$) and 5.5 per cent at 150 km depth ($\Delta T \approx 300\,^{\circ}\mathrm{C}$). In our tomographic images of V_{S} we find a maximum relative anomaly between southeast and northwest of around 7.5 per cent at 100 km depth and around 5 per cent at 150 km depth (Fig. 5).

Using a more complete 3-D modelling approach of the lithosphere in southwestern Scandinavia, Gradmann *et al.* (2013) estimated an abrupt change in lithospheric thickness from 100 to 200 km across the Oslo Graben, but also needed a change in composition between a fertile southern Norwegian mantle and a depleted Fennoscandian Shield to fit absolute V_{SV} velocities in southern Norway (Maupin 2011) and Sweden (Cotte & Pedersen 2002).

Both modelling approaches show that a lithosphere in local isostatic equilibrium can exhibit strong variations in seismic velocities just from variations in lithospheric thickness and associated temperature variations. It is therefore not necessary to invoke a plume or diapir in the uppermost mantle below southern Norway (Rohrman & van der Beek 1996; Rohrman *et al.* 2002) to explain the low

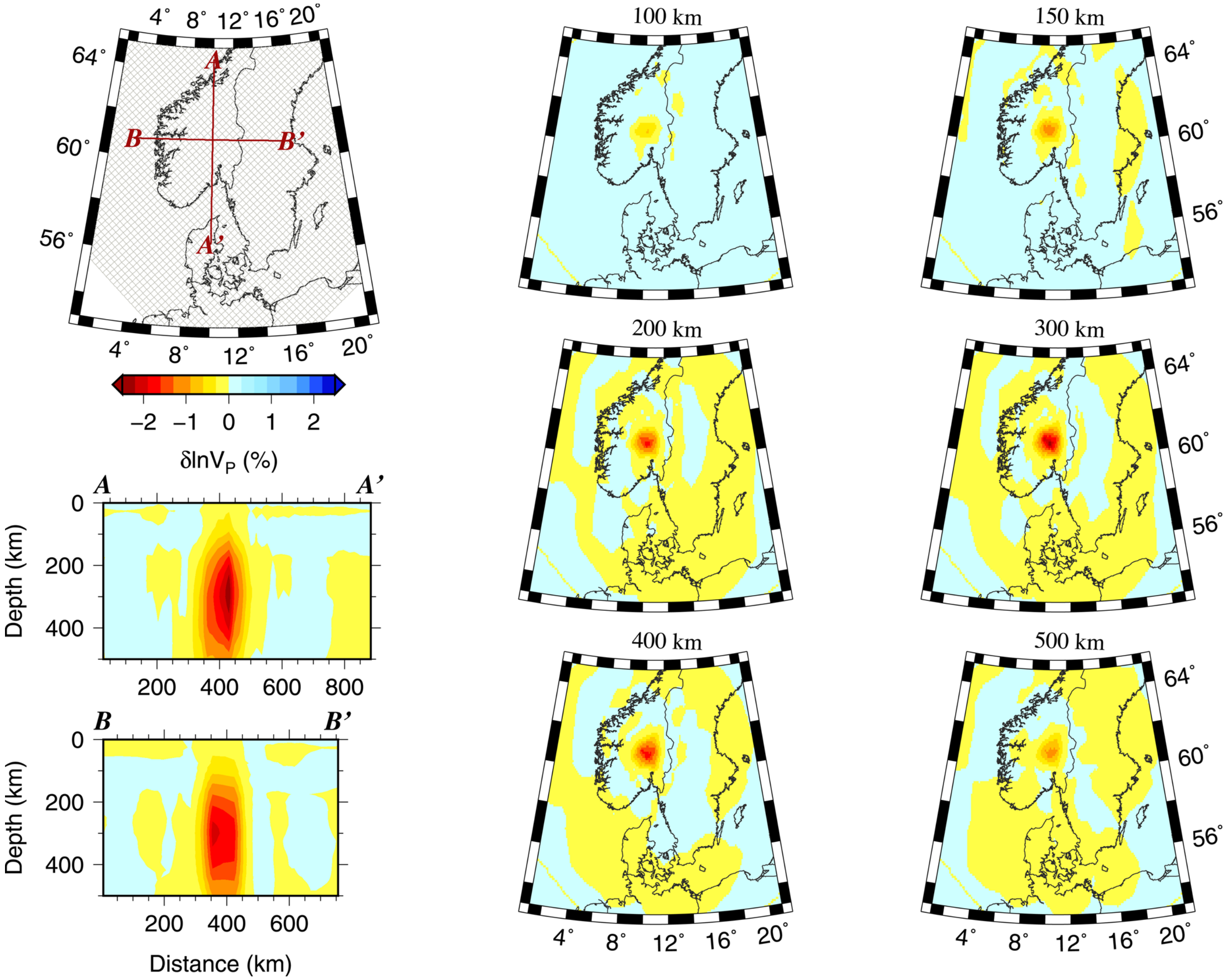

Figure 24. Recovered *P*-wave model using the 3-D multiscale parametrization with the synthetic model shown in Fig. 23 and a velocity perturbation $\delta ln V_P = -3$ per cent. Upper left map shows location of profiles and grid discretization.

seismic velocities. A direct translation of the relative velocity anomalies in Figs 4 and 5 into relative temperature anomalies could easily be taken as evidence for anomalously hot temperatures and diapiric upwelling of the asthenosphere into the lithosphere.

Neither the lithospheric modelling of Kolstrup *et al.* (2012) nor Gradmann *et al.* (2013) is able to explain the details in our tomographic images, but suggests that the low velocities in the channel-like structure between Denmark and Norway may be due to a thin but stable lithosphere of about 100 km overlying convecting asthenosphere. The high velocities in Sweden and the sharp transition from low to high velocities can likewise be explained by a rapid increase in lithospheric thickness, possibly associated with a higher degree of depletion of the lithospheric mantle below Sweden.

What we cannot explain by variations in lithospheric thickness and mantle depletion is the deep cylindrical low-velocity anomaly that does not fit at all with the uniform asthenosphere assumed below the lithosphere in Kolstrup *et al.* (2012) and Gradmann *et al.* (2013). Above 200 km depth, the cylinder merges with the low-velocity channel and could be ascribed to lithospheric thickness variations, but between depths of 200 and 350 km it is a much stronger feature than the deep part of the channel and it has its own distinct geometry. The location of the structure is slightly west of the northern end of the Oslo Graben and it might therefore have an origin in the extensive Permian magmatism of the Oslo Graben (Neumann *et al.* 2004; Larsen *et al.* 2008; Torsvik *et al.* 2008).

The perhaps most natural explanation for such a structure is a centralized small-scale upwelling, but numerical simulations using a uniform composition for the asthenosphere indicate that upwelling would not give a velocity anomaly as strong as −3 per cent in V_S and 1.5–2 per cent in V_P (Hieronymus *et al.* 2007). Hence, the narrow cylinder needs to be anomalously hot or to have an anomalous composition, with for example a higher water content or increased heat production.

The interpretations in this section are based mainly on the anomalies in V_S. The covariation of V_P and V_S in $\delta ln(V_P/V_S)$ provides additional information on the causes of the velocity anomalies, especially on compositional variations, and will be explored in the following section.

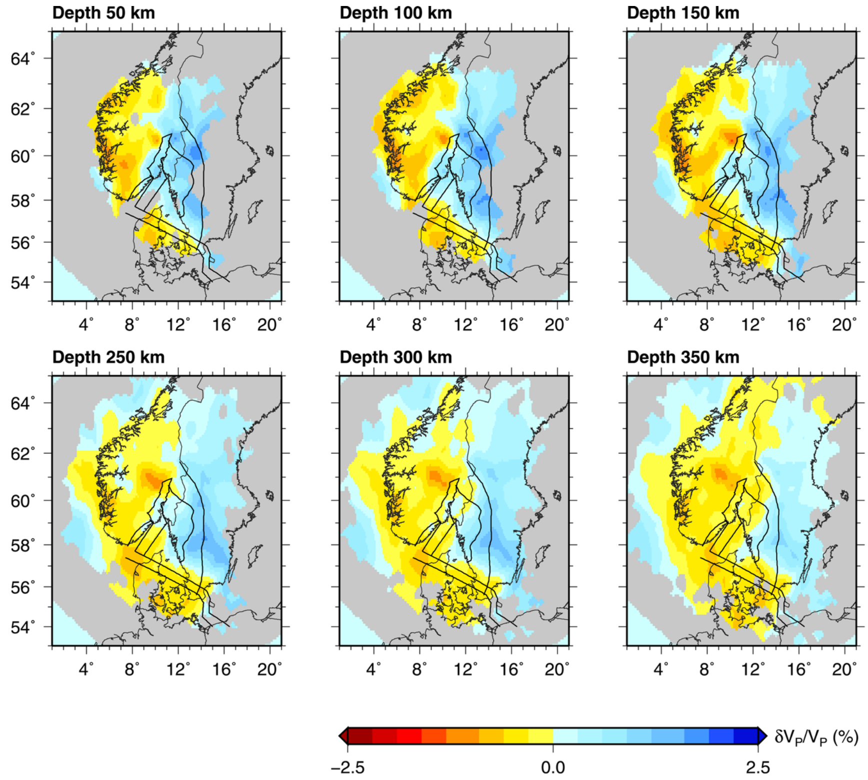

Figure 25. The same as Fig. 4 for the δlnV_{P} model obtained using only the high-frequency *P*-wave data set and a ray-theoretical approach. The same 3-D multiscale parametrization and damping value as in Fig. 4 is used in the inversion.

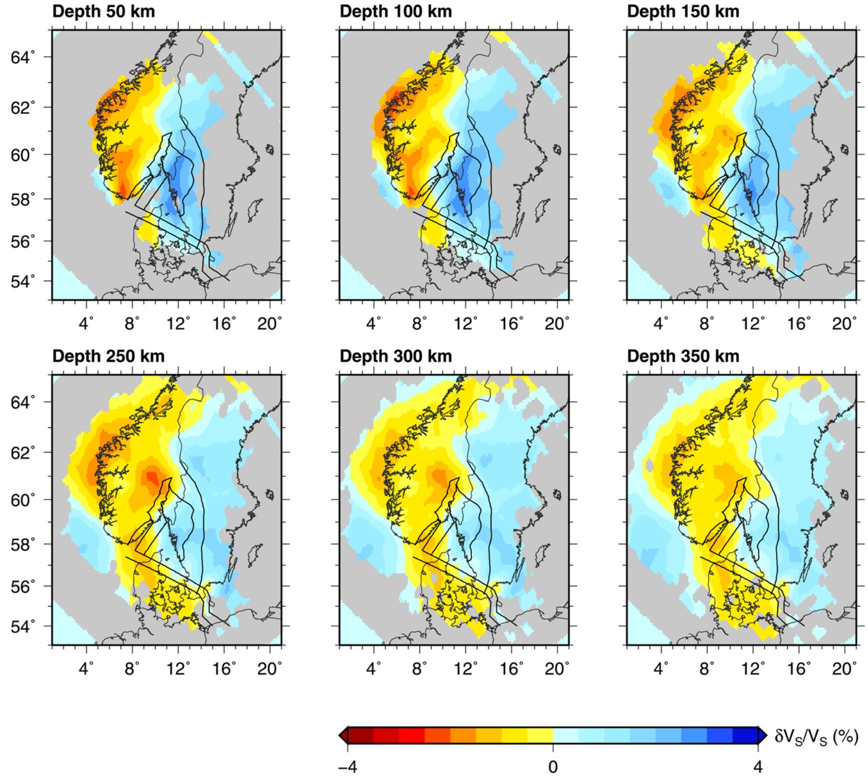

Figure 26. The same as Fig. 5 for the δlnV_{S} model obtained using only the high-frequency *S*-wave data set and a ray-theoretical approach. The same 3-D multiscale parametrization and damping value as in Fig. 5 is used in the inversion.

5.4 Tectonophysical implications—$\delta ln(V_P/V_S)$ and compositional variation

Many workers infer a variation of the subcontinental mantle composition with time; the oldest Archean compositions being more depleted in basaltic components (especially iron) than the Proterozoic, and the younger Phanerozoic compositions being the most fertile. Variations in iron content, or Mg# (atomic ratio 100 × Mg/Mg + Fe), are caused by different degrees of melt extraction and refertilization from metasomatism (e.g. Poudjom Djomani *et al.* 2001; Griffin *et al.* 2009). The depletion of old cratonic mantle contributes its higher velocities and to its tectonic stability (e.g. Jordan 1988; Poudjom Djomani *et al.* 2001).

Modelling also shows that the compositional difference between depleted and fertile lithospheric mantle, though it does not contribute much in itself to velocity variations, can be crucial for the long-term stability of variations in lithospheric thickness and hence contribute to lateral contrasts in temperature and seismic velocities (Hieronymus *et al.* 2007). In addition, variations in heat production between fertile and depleted mantle might be an overlooked contributor to seismic velocity anomalies in the subcontinental lithospheric mantle (Hieronymus & Goes 2010).

The variation in V_P/V_S is estimated to be a fairly strong indicator of compositional variations in Mg#, with high values of V_P/V_S being associated with low Mg# and a fertile mantle, and with low values of V_P/V_S being associated with high Mg# and depleted mantle (Lee 2003). We can therefore use the covariation of $\delta ln V_P$ and $\delta ln V_S$ to get an independent estimate of the degree of depletion inferred by Gradmann *et al.* (2013).

We estimate negative anomalies in $\delta ln(V_P/V_S)$ of up to −3 per cent in Sweden and positive anomalies up to +2 per cent in southern Norway and Denmark, but most of the values are in the range ±1.5 per cent (Fig. 9). Below the Oslo Graben we find a positive anomaly of +2 per cent at depths from 200 to 350 km.

The anomalies in V_P/V_S are relative variations with respect to the unknown 1-D mean in our study area. We assume that we can use the regional mean V_P/V_S for Western Europe estimated by Artemieva (2007) from global absolute tomographies (Bijwaard & Spakman 2000; Shapiro & Ritzwoller 2002). At 150 km depth, where the resolution of both the *P*- and *S*-wave tomography is good, the average V_P/V_S ratio is estimated to be 1.73 ± 0.04 (Artemieva 2007). Taking this value as our regional mean at 150 km depth, the minimum anomalies of ±1 per cent give a minimum change in V_P/V_S from 1.71 below Sweden to 1.75 below southern Norway. Using the relationship in Lee (2003), this change corresponds to a change in Mg# from a depleted composition (Mg# 93) to an unrealistically fertile composition (Mg# 84).

The relationship of V_P/V_S found in Lee (2003) has been questioned as it is an extrapolation based on data measured at standard pressure and temperature and does not take into account anelastic effects and phase transitions (Afonso *et al.* 2010). Afonso *et al.* (2010) find that the relationship between V_P/V_S and Mg# is valid only for garnet bearing assemblages below 900 °C as anelastic effects makes the V_P/V_S ratio strongly dependent on temperature at high temperatures. The high V_P/V_S anomalies below southern Norway can therefore be explained by temperature alone and following Afonso *et al.* (2010) by a temperature anomaly of about +300 °C. In Sweden though, the anharmonic V_P/V_S relationship should still hold down to depths of 100–150 km, as temperatures are estimated to be below 1000 °C and garnet stable (Afonso *et al.* 2010; Gradmann *et al.* 2013). The negative anomalies in $\delta ln(V_P/V_S)$ between −1 and −3 per cent at 50–150 km depth are therefore indicative of a depleted mantle with high Mg#.

It should be noted that Afonso *et al.* (2010) estimate the compositional difference between a standard tectonic and Proterozoic lithosphere to be quite small, giving variations in $\delta(V_P/V_S)$ of approximately 0.01 that corresponds to anomalies of about 0.6 per cent in $\delta ln(V_P/V_S)$. Hence, the V_P/V_S anomalies in this study are too large to be explained by variations in Mg# alone, and temperature must account for some of the variation. As depletion in iron content (increase in Mg#) is associated with depletion in heat productive radiogenic elements leading to thermal anomalies of up to 100–300 °C (Hieronymus & Goes 2010), variations in the V_P/V_S ratio due to the total effect of compositional variations in a heterogeneous mantle might be underestimated in the modelling of Afonso *et al.* (2010). Variations in heat production associated with depletion of the mantle might therefore explain some of the west to east variation in V_P/V_S in our images.

Artemieva (2007) points out that the ratio V_P/V_S estimated from global studies is not sensitive to compositional variations between lithospheres of age older than 0.9 Ga, but is effective in delineating the outline of the continental shield mantle. Hence, despite the limitations in use of the V_P/V_S ratio, the covariation of $\delta ln V_P$ and $\delta ln V_S$ in our images effectively places southern Norway and Denmark outside the Fennoscandian Shield and indicates a strongly depleted shield mantle in Sweden.

5.5 Relation to topography and dynamic models

We find, as previous studies, a lateral mantle boundary coinciding with the Sorgenfrei-Tornquist Zone (STZ) in Denmark and southern Sweden (Fig. 1). The STZ continues as the Tornquist-Teisseyre Zone (TTZ) southeast of our study area, where it separates Phanerozoic Europe from the Precambrian Easteuropean Platform. Both the STZ (Cotte & Pedersen 2002; Shomali & Roberts 2002; Shomali *et al.* 2006) and TTZ (Zielhuis & Nolet 1994; Janutyte *et al.* 2014) are associated with a strong lateral boundary in the upper mantle.

Across the STZ, crustal studies show an increase in Moho depth, both in the Skagerrak Sea (Lie & Andersson 1998), in Denmark (Thybo 2001), and in southern Sweden (Thybo 2001). The STZ is, despite the change in crustal thickness, not associated with any marked change in topography.

The STZ and the Skagerrak and Oslo Grabens have a common origin in Carboniferous-Permian extensional tectonics and extensive magmatic activity (Thybo 2001; Neumann *et al.* 2004; Larsen *et al.* 2008). Despite this, the lateral mantle boundary was expected to continue westwards and not to take a detour into southern Norway following the graben structures, as the extensively reworked Danish Basin (e.g. Thybo 2001) has a very different crustal structure than the thicker crust of southern Norway (e.g. Stratford & Thybo 2011). Where the lateral mantle boundary branches north from the Oslo Graben, it is no longer associated with any major crustal structures at the surface. On the contrary, the boundary crosses the north-east trending Caledonides and the Scandinavian Mountains (Fig. 1).

Using the STZ as an example, Hieronymus *et al.* (2007) modelled how edge-driven convection would evolve between lithospheres of contrasting thickness (100 and 250 km) and composition (pyrolite and harzburgite) since the last Triassic rifting events 220 Ma. The modelling is able to explain the sharp lateral contrast in seismic velocities across the STZ due to a stable convection pattern. The modelling also shows that the difference in lithospheric thickness is not necessarily associated with any discernible change in surface heat flow, and that the high viscosity of the thicker and older lithosphere stabilizes it against erosion.

The model of Hieronymus *et al.* (2007) is compatible with the increase in lithospheric thickness inferred from lithospheric modelling in southern Norway (Kolstrup *et al.* 2012; Gradmann *et al.* 2013) and explains how such a configuration of the lithosphere can be stable over time. Pascal *et al.* (2004) suggest that the Oslo Graben developed at the edge of an already existing stepwise increase in lithospheric thickness. It is therefore possible that the sharp contrast in seismic velocities in the upper 50–250 km dates back to even older tectonic events than the Carboniferous-Permian rifting.

Another possible scenario is that the rifting left the originally thick (200 km?) shield mantle below southern Norway partly rehydrated and refertilized. Rehydration can effectively weaken lithospheric mantle, as seen in for example mantle xenoliths of the Proterozoic Colorado Plateau (Li *et al.* 2008). A lithospheric step would in this case have existed between the Danish Basin and southern Norway, facilitating edge-driven convection. Dynamic modelling shows that small-scale edge-driven convection can erode fertile and hydrated lithosphere (Hieronymus *et al.* 2007; Van Wijk *et al.* 2010; Kaislaniemi & van Hunen 2014). Lithospheric erosion by edge-driven convection has been used to explain Cenozoic episodic uplift and magmatism in for example the Atlas Mountains (Kaislaniemi & van Hunen 2014) and the Colorado Plateau (Van Wijk *et al.* 2010). Furthermore, the opening of the North Atlantic and the Icelandic plume could also have triggered convection and erosion of the southern Norwegian mantle, as regional tomographies point to a connection between the Iceland plume and southern Norway (Weidle & Maupin 2008; Rickers *et al.* 2013).

Hence, episodic erosion of an initially thick shield mantle below southern Norway to its current thickness of about 100 km could explain some of the episodic uplift inferred from geological observations throughout the Mesozoic and Cenozoic in this area (Gabrielsen *et al.* 2010). Nielsen *et al.* (2002) estimate that delamination of 35 km of lithospheric mantle will result in a long-lived uplift greater than 500 m of the average surface. A thin and weak lithosphere is also a necessary prerequisite for uplift from other mechanisms such as lithospheric folding due to far-field compressional stresses (Doré *et al.* 2008; Cloetingh & Burov 2011).

Japsen *et al.* (2012) reject edge-driven convection as a possible contributor to the topography of elevated passive continental margins but do not consider newer modelling (e.g. Hieronymus *et al.* 2007; Van Wijk *et al.* 2010; Kaislaniemi & van Hunen 2014) performed after the original work of King & Anderson (1998). They find that only far-field compressive stresses and lithospheric folding can explain their observations of uplift in areas such as southern Norway and eastern Greenland. Our images of strongly varying lithospheric properties suggest that the structure and evolution of the mantle must be taken into account as well, and modelling of edge-driven convection points to the importance of erosive weakening of continental margins. Episodic erosion of the lithosphere could act as a trigger of uplift events and weaken the lithospheric margin, facilitating uplift due to compressive stresses.

6 CONCLUSIONS

We present the first finite-frequency *P*- and *S*-wave tomographies in southwestern Scandinavia, using a wavelet-based multiscale parametrization that greatly increases the recovery of amplitude and location of seismic velocity anomalies.

We image, as previous studies, low velocities in both V_P and V_S below southern Norway and Denmark compared to high velocities below Sweden and towards the central Fennoscandian Shield, but add to this picture important details. The low-velocity region below southern Norway consists of two adjacent anomalies: a shallow channel-like feature extending from the coastal and western part of southern Norway into Denmark, and a cylindrically shaped anomaly that emerges from the channel further east at 150–200 km depth and extends to a depth of around 350 km. Furthermore, we find that the lateral boundary between the low and high velocities closely follows Carboniferous-Permian rift structures and centres of magmatic activity, that is the Sorgenfrei-Tornquist Zone and the Oslo Rift. Anomalies in the V_P/V_S ratio are robustly constrained in the upper part of the model but depth variations cannot be imaged with confidence. Below Sweden we estimate negative anomalies in the V_P/V_S ratio down to -3 per cent and below southern Norway positive anomalies up to $+2$ per cent.

The variations in δlnV_P, δlnV_S and $\delta ln(V_P/V_S)$ point consistently to higher temperatures below southern Norway and Denmark compared to Sweden and also to a higher degree of depletion in the lithospheric mantle below Sweden. The low velocities and higher temperatures in Denmark and Norway can be explained to a large part simply by a thinner lithosphere, but the deeper cylindrical low-velocity anomaly below the northwestern end of the Oslo Graben is more difficult to explain.

The channel-like low-velocity region is associated with a high degree of intraplate seismicity and an estimated contribution to the support of the high topography by low density material in the uppermost mantle. It is possible that the thin lithosphere below southern Norway and the stepwise increase in thickness towards the central Fennoscandian Shield is older than the Carboniferous-Permian rifting. On the other hand, it is equally possible that an originally thick but weakened lithosphere has been eroded to its current thickness of about 100 km after the Permian, causing episodic uplift of the area.

ACKNOWLEDGEMENTS

This work has been done in the framework of the ESF EUROCORES TOPO-EUROPE Program 07-TOPO-EUROPE-FP-014 and was supported by MOST grant,102-2116-M-002-025, in Taiwan (S.-H. Hung). MAGNUS waveforms were recorded with the mobile KArlsruhe BroadBand Array (KABBA) of the Karlsruhe Institute of Technology, Germany as well as with permanent stations of the NORSAR array and the Norwegian National Seismological Network. We thank Andy Frassetto for providing us with the DANSEIS data (University of Copenhagen) and Marie Keiding (Geological Survey of Norway) for helping with the FENCAT database. We are grateful to Niels Balling (Univerity of Aarhus) for sharing data from the CALAS experiment with us. Seismological stations of the CALAS project, applied in this study, were from the University of Aarhus instrument pool and from the NERC Geophysical Equipment Facility (SEIS-UK). That project was financially supported by the Danish National Science Research Council. Financial support for the MAGNUS experiment was provided by the Universities of Aarhus, Copenhagen, Karlsruhe and Oslo as well as NORSAR. This work greatly improved from the constructive reviews of Karin Sigloch and an anonymous reviewer. Figures have been prepared using the Generic Mapping Tools (Wessel & Smith 1998) and M_Map (Pawlowicz 2005).

REFERENCES

Afonso, J.C., Ranalli, G., Fernàndez, M., Griffin, W.L., O'Reilly, S.Y. & Faul, U., 2010. On the Vp/Vs–Mg# correlation in mantle peridotites: implications for the identification of thermal and compositional anomalies in the upper mantle, *Earth planet. Sci. Lett.,* **289**(3), 606–618.

Aki, K., Christoffersson, A. & Husebye, E.S., 1977. Determination of the three-dimensional seismic structure of the lithosphere, *J. geophys. Res.,* **82**(2), 277–296.

Artemieva, I.M., 2007. Dynamic topography of the East European craton: shedding light upon lithospheric structure, composition and mantle dynamics, *Glob. Planet Change,* **58**(1), 411–434.

Assumpção, M., Schimmel, M., Escalante, C., Barbosa, J.R., Rocha, M. & Barros, L.V., 2004. Intraplate seismicity in SE Brazil: stress concentration in lithospheric thin spots, *Geophys. J. Int.,* **159**(1), 390–399.

Berckhemer, H., Kampfmann, W., Aulbach, E. & Schmeling, H., 1982. Shear modulus and Q of forsterite and dunite near partial melting from forced-oscillation experiments, *Phys. Earth planet. Inter.,* **29**(1), 30–41.

Bijwaard, H. & Spakman, W., 2000. Non-linear global P-wave tomography by iterated linearized inversion, *Geophys. J. Int.,* **141**(1), 71–82.

Bingen, B. *et al.*, 2005. Timing of continental building in the Sveconorwegian orogen, SW Scandinavia, *Norw. J. Geol.,* **85,** 87–116.

Bungum, H., Olesen, O., Pascal, C., Gibbons, S., Lindholm, C. & Vestøl, O., 2010. To what extent is the present seismicity of Norway driven by post-glacial rebound?, *J. geol. Soc.,* **167**(2), 373–384.

Cammarano, F., Goes, S., Vacher, P. & Giardini, D., 2003. Inferring upper-mantle temperatures from seismic velocities, *Phys. Earth planet. Inter.,* **138**(3), 197–222.

Charléty, J., Voronin, S., Nolet, G., Loris, I., Simons, F.J., Sigloch, K. & Daubechies, I.C., 2013. Global seismic tomography with sparsity constraints: comparison with smoothing and damping regularization, *J. geophys. Res.,* **118**(9), 4887–4899.

Chevrot, S. & Zhao, L., 2007. Multiscale finite-frequency rayleigh wave tomography of the kaapvaal craton, *Geophys. J. Int.,* **169**(1), 201–215.

Chevrot, S., Martin, R. & Komatitsch, D., 2012. Optimized discrete wavelet transforms in the cubed sphere with the lifting scheme—implications for global finite-frequency tomography, *Geophys. J. Int.,* **191**(3), 1391–1402.

Chiao, L.-Y. & Kuo, B.-Y., 2001. Multiscale seismic tomography, *Geophys. J. Int.,* **145**(2), 517–527.

Chiao, L.-Y. & Liang, W.-T., 2003. Multiresolution parameterization for geophysical inverse problems, *Geophysics,* **68**(1), 199–209.

Chiao, L.-Y., Lin, J.-R. & Gung, Y.-C., 2006. Crustal magnetization equivalent source model of Mars constructed from a hierarchical multiresolution inversion of the Mars Global Surveyor data, *J. geophys. Res.,* **111,** E12010, doi:10.1029/2006JE002725.

Chiao, L.-Y., Fang, H.-Y., Gung, Y.-C., Chang, Y.-H. & Hung, S.-H., 2010. Comparative appraisal of linear inverse models constructed via distinctive parameterizations (comparing distinctly inverted models), *J. geophys. Res.,* **115,** B07305, doi:10.1029/2009JB006867.

Chou, H.-C., Kuo, B.-Y., Chiao, L.-Y., Zhao, D. & Hung, S.-H., 2009. Tomography of the westernmost Ryukyu subduction zone and the serpentinization of the fore-arc mantle, *J. geophys. Res.,* **114,** B12301, doi:10.1029/2008JB006192.

Cloetingh, S. & Burov, E., 2011. Lithospheric folding and sedimentary basin evolution: a review and analysis of formation mechanisms, *Basin Res.,* **23**(3), 257–290.

Cocks, L. & Torsvik, T., 2006. European geography in a global context from the Vendian to the end of the Palaeozoic, in *European Lithosphere Dynamics,* Vol. 32 of Geol. Soc. Lond. Mem., pp. 83–95, eds Gee, D. & Stephenson, R., Geological Society.

Cohen, A., Daubechies, I. & Feauveau, J.-C., 1992. Biorthogonal bases of compactly supported wavelets, *Commun. Pure appl. Math.,* **45**(5), 485–560.

Cotte, N. & Pedersen, H., 2002. Sharp contrast in lithospheric structure across the Sorgenfrei–Tornquist Zone as inferred by Rayleigh wave analysis of TOR1 project data, *Tectonophysics,* **360**(1), 75–88.

Dahlen, F., Hung, S.-H. & Nolet, G., 2000. Fréchet kernels for finite-frequency traveltimes—Theory, I., *Geophys. J. Int.,* **141**(1), 157–174.

Doré, A., Lundin, E., Kusznir, N. & Pascal, C., 2008. Potential mechanisms for the genesis of Cenozoic domal structures on the NE Atlantic margin: pros, cons and some new ideas, *Geol. Soc. Lond. Spec. Publ.,* **306**(1), 1–26.

Ebbing, J., England, R., Korja, T., Lauritsen, T., Olesen, O., Stratford, W. & Weidle, C., 2012. Structure of the Scandes lithosphere from surface to depth, *Tectonophysics,* **536,** 1–24.

Euler, G., 2014. Project SEIZMO, Available at: http://epsc.wustl.edu/~ggeuler/codes/m/seizmo/, last accessed 5 January 2014.

FENCAT, 2011. Institute of Seismology, University of Helsinki, Available at: http://www.helsinki.fi/geo/seismo/english/bulletins/index.html, last accessed 16 January 2015.

Fichtner, A., Saygin, E., Taymaz, T., Cupillard, P., Capdeville, Y. & Trampert, J., 2013. The deep structure of the North Anatolian Fault Zone, *Earth planet. Sci. Lett.,* **373,** 109–117.

Frasetto, A. & Thybo, H., 2013. Receiver function analysis of the crust and upper mantle in Fennoscandia—isostatic implications, *Earth planet. Sci. Lett.,* **381,** 234–246.

Frederiksen, S., Nielsen, S.B. & Balling, N., 2001. A numerical dynamic model for the Norwegian–Danish Basin, *Tectonophysics,* **343**(3), 165–183.

Gaál, G. & Gorbatschev, R., 1987. An outline of the Precambrian evolution of the Baltic Shield, *Precambrian Res.,* **35,** 15–52.

Gabrielsen, R.H., Faleide, J.I., Pascal, C., Braathen, A., Nystuen, J.P., Etzelmuller, B. & O'Donnell, S., 2010. Latest Caledonian to Present tectonomorphological development of southern Norway, *Mar. Petrol. Geol.,* **27**(3), 709–723, The link between shallow and deep processes in sedimentary basins.

Goes, S., Govers, R. & Vacher, P., 2000. Shallow mantle temperatures under Europe from P and S wave tomography, *J. geophys. Res.,* **105**(B5), 11 153–11 169.

Gradmann, S., Ebbing, J. & Fullea, J., 2013. Integrated geophysical modelling of a lateral transition zone in the lithospheric mantle under Norway and Sweden, *Geophys. J. Int.,* **194**(3), 1359–1374.

Griffin, W., O'Reilly, S.Y., Afonso, J.C. & Begg, G., 2009. The composition and evolution of lithospheric mantle: a re-evaluation and its tectonic implications, *J. Petrol.,* **50**(7), 1185–1204.

Hieronymus, C. & Goes, S., 2010. Complex cratonic seismic structure from thermal models of the lithosphere: effects of variations in deep radiogenic heating, *Geophys. J. Int.,* **180**(3), 999–1012.

Hieronymus, C.F., Shomali, Z.H. & Pedersen, L.B., 2007. A dynamical model for generating sharp seismic velocity contrasts underneath continents: application to the Sorgenfrei–Tornquist Zone, *Earth planet. Sci. Lett.,* **262**(1), 77–91.

Högdahl, K., Andersson, U. & Eklund, O., 2004. *The Transscandinavian Igneous Belt (TIB) in Sweden: A Review of Its Character and Evolution,* Vol. 37 of Special Paper, Geological Survey of Finland.

Hung, S.-H., Shen, Y. & Chiao, L.-Y., 2004. Imaging seismic velocity structure beneath the Iceland hot spot: a finite frequency approach, *J. geophys. Res.,* **109,** B08305, doi:10.1029/2003JB002889.

Hung, S.-H., Chen, W.-P., Chiao, L.-Y. & Tseng, T.-L., 2010. First multiscale, finite-frequency tomography illuminates 3-D anatomy of the Tibetan Plateau, *Geophys. Res. Lett.,* **37,** L06304, doi:10.1029/2009GL041875.

Hung, S.-H., Chen, W.-P. & Chiao, L.-Y., 2011. A data-adaptive, multiscale approach of finite-frequency, traveltime tomography with special reference to P and S wave data from central Tibet, *J. geophys. Res.,* **116,** B06307, doi:10.1029/2010JB008190.

Jackson, I., Fitz Gerald, J.D., Faul, U.H. & Tan, B.H., 2002. Grain-size-sensitive seismic wave attenuation in polycrystalline olivine, *J. geophys. Res.,* **107**(B12), 2360, doi:10.1029/2001JB001225.

Janutyte, I. *et al.*, 2014. Upper mantle structure around the Trans-European Suture Zone obtained by teleseismic tomography, *Solid Earth Discussions,* **6**(2), 1723–1763.

Japsen, P. & Chalmers, J.A., 2000. Neogene uplift and tectonics around the North Atlantic: overview, *Glob. Planet. Change,* **24**(3-4), 165–173.

Japsen, P., Chalmers, J.A., Green, P.F. & Bonow, J.M., 2012. Elevated, passive continental margins: not rift shoulders, but expressions of episodic, post-rift burial and exhumation, *Glob. Planet Change,* **90,** 73–86.

Jones, S.M., White, N., Clarke, B.J., Rowley, E. & Gallagher, K., 2002. Present and past influence of the Iceland Plume on sedimentation, *Geol. Soc. Lond. Spec. Publ.,* **196**(1), 13–25.

Jordan, T.H., 1988. Structure and formation of the continental tectosphere, *J. Petrol.*, (1), 11–37.

Kaislaniemi, L. & van Hunen, J., 2014. Dynamics of lithospheric thinning and mantle melting by edge-driven convection: application to Moroccan Atlas mountains, *Geochem. Geophys. Geosyst.,* **15,** 3175–3189.

Kennett, B. & Gudmundsson, O., 1996. Ellipticity corrections for seismic phases, *Geophys. J. Int.,* **127**(1), 40–48.

Kennett, B., Widiyantoro, S. & Hilst, R.v.d., 1998. Joint seismic tomography for bulk sound and shear wave speed in the Earth's mantle, *J. geophys. Res.,* **103**(B6), 12 469–12 493.

Kennett, B.L.N., Engdahl, E.R. & Buland, R., 1995. Constraints on seismic velocities in the Earth from traveltimes, *Geophys. J. Int.,* **122**(1), 108–124.

King, S.D. & Anderson, D.L., 1998. Edge-driven convection, *Earth planet. Sci. Lett.,* **160**(3), 289–296.

Köhler, A., Weidle, C. & Maupin, V., 2012. Crustal and uppermost mantle structure of southern Norway: results from surface wave analysis of ambient seismic noise and earthquake data, *Geophys. J. Int.,* **191**(3), 1441–1456.

Kolstrup, M., 2015. Old sutures and young plumes?—New geophysical investigations of the crust and upper mantle in southwestern Scandinavia, *PhD thesis,* University of Oslo.

Kolstrup, M.L. & Maupin, V., 2013. A Proterozoic boundary in southern Norway revealed by joint-inversion of P-receiver functions and surface waves, *Precambrian Res.,* **238,** 186–198.

Kolstrup, M.L., Pascal, C. & Maupin, V., 2012. What compensates the topography of southern Norway? Insights from thermo-isostatic modeling, *J. Geodyn.,* **61,** 105–119.

Larsen, B.T., Olaussen, S., Sundvoll, B. & Heeremans, M., 2008. The Permo-Carboniferous Oslo Rift through six stages and 65 million years, *Episodes,* **31**(1), 52–58.

Lee, C.-T.A., 2003. Compositional variation of density and seismic velocities in natural peridotites at STP conditions: implications for seismic imaging of compositional heterogeneities in the upper mantle, *J. geophys. Res.,* **108**(B9), doi:10.1029/2003JB002413.

Li, Z.-X.A., Lee, C.-T.A., Peslier, A.H., Lenardic, A. & Mackwell, S.J., 2008. Water contents in mantle xenoliths from the Colorado Plateau and vicinity: implications for the mantle rheology and hydration-induced thinning of continental lithosphere, *J. geophys. Res.,* **113,** B09210, doi:10.1029/2007JB005540.

Lidmar-Bergstrom, K. & Bonow, J.M., 2009. Hypotheses and observations on the origin of the landscape of southern Norway—a comment regarding the isostasy-climate-erosion hypothesis by Nielsen et al. 2008, *J. Geodyn.,* **48**(2), 95–100.

Lie, J. & Andersson, M., 1998. The deep-seismic image of the crustal structure of the Tornquist Zone beneath the Skagerrak Sea, northwestern Europe, *Tectonophysics,* **287**(1), 139–155.

Lindholm, C.D., Bungum, H., Hicks, E. & Villagran, M., 2000. Crustal stress and tectonics in Norwegian regions determined from earthquake focal mechanisms, *Geol. Soc. Lond. Spec. Publ.,* **167**(1), 429–439.

Loris, I., Nolet, G., Daubechies, I. & Dahlen, F., 2007. Tomographic inversion using l1-norm regularization of wavelet coefficients, *Geophys. J. Int.,* **170**(1), 359–370.

Loris, I., Douma, H., Nolet, G., Daubechies, I. & Regone, C., 2010. Nonlinear regularization techniques for seismic tomography, *J. Comput. Phys.,* **229**(3), 890–905.

Lou, X., van der Lee, S. & Lloyd, S., 2013. AIMBAT: a Python/Matplotlib tool for measuring teleseismic arrival times, *Seism. Res. Lett.,* **84**(1), 85–93.

Martin, M. *et al.* 2005. High-resolution teleseismic body-wave tomography beneath SE Romania–I. Implications for three-dimensional versus one-dimensional crustal correction strategies with a new crustal velocity model, *Geophys. J. Int.,* **162**(2), 448–460.

Maupin, V., 2011. Upper-mantle structure in southern Norway from beamforming of Rayleigh wave data presenting multipathing, *Geophys. J. Int.,* **185**(2), 985–1002.

Maupin, V. & Kolstrup, M., 2015. Insights in P and S relative travel time tomography from analyzing finite-frequency Fréchet kernels, *Geophys. J. Int.,* submitted.

Maupin, V. *et al.*, 2013. The deep structure of the Scandes and its relation to tectonic history and present-day topography, *Tectonophysics,* **602,** 15–37.

Medhus, A., Balling, N., Jacobsen, B., Weidle, C., England, R., Kind, R., Thybo, H. & Voss, P., 2012. Upper-mantle structure beneath the Southern Scandes Mountains and the Northern Tornquist Zone revealed by P-wave traveltime tomography, *Geophys. J. Int.,* **189**(3), 1315–1334.

Medhus, A.B., Balling, N., Jacobsen, B.H., Kind, R. & England, R.W., 2009. Deep-structural differences in southwestern Scandinavia revealed by P-wave travel time residuals, *Norw. J. Geol.,* **89,** 203–214.

Menke, W., 1984. *Geophysical Data Analysis: Discrete Inverse Theory,* Academic Press.

Meyerholtz, K.A., Pavlis, G.L. & Szpakowski, S.A., 1989. Convolutional quelling in seismic tomography, *Geophysics,* **54**(5), 570–580.

Neumann, E., Wilson, M., Heeremans, M., Spencer, E., Obst, K., Timmerman, M. & Kirstein, L., 2004. Carboniferous-Permian rifting and magmatism in southern Scandinavia, the North Sea and northern Germany: a review, *Geol. Soc. Lond. Spec. Publ.,* **223**(1), 11–40.

Nielsen, S.B. *et al.*, 2002. Paleocene initiation of Cenozoic uplift in Norway, *Geol. Soc. Lond. Spec. Publ.,* **196**(1), 45–65.

Nielsen, S.B., Gallagher, K., Egholm, D.L., Clausen, O.R. & Summerfield, M., 2009a. Reply to comment regarding the ICE-hypothesis, *J. Geodyn.,* **48**(2), 101–106.

Nielsen, S.B. *et al.*, 2009b. The evolution of western Scandinavian topography: a review of Neogene uplift versus the ICE (isostasy-climate-erosion) hypothesis, *J. Geodyn.,* **47**(2-3), 72–95.

Nironen, M., 1997. The Svecofennian Orogen: a tectonic model, *Precambrian Res.,* **86**(1), 21–44.

Nolet, G., 2008. *A Breviary of Seismic Tomography: Imaging the Interior of the Earth and Sun,* Cambridge Univ. Press.

Obayashi, M., Suetsugu, D. & Fukao, Y., 2004. PP-P differential traveltime measurement with crustal correction, *Geophys. J. Int.,* **157**(3), 1152–1162.

Pascal, C. & Olesen, O., 2009. Are the Norwegian mountains compensated by a mantle thermal anomaly at depth?, *Tectonophysics,* **475**(1), 160–168.

Pascal, C., Cloetingh, S. & Davies, G., 2004. Asymmetric lithosphere as the cause of rifting and magmatism in the Permo-Carboniferous Oslo Graben, in *Permo-Carboniferous Magmatism and Rifting in Europe,* Vol. 223, pp. 139–156, eds Wilson, M., Neumann, E.-R., Davies, G., Timmerman, M., Heeremans, M. & Larsen, B.T., Geol. Soc. Lond. Spec. Publ.

Pawlowicz, R., 2005. M_Map: a mapping package for Matlab, Available at: http://www.eos.ubc.ca/~rich/map.html, last accessed 5 January 2014.

Poudjom Djomani, Y.H., O'Reilly, S.Y., Griffin, W. & Morgan, P., 2001. The density structure of subcontinental lithosphere through time, *Earth planet. Sci. Lett.,* **184**(3), 605–621.

Rickers, F., Fichtner, A. & Trampert, J., 2013. The Iceland–Jan Mayen plume system and its impact on mantle dynamics in the North Atlantic region: evidence from full-waveform inversion, *Earth planet. Sci. Lett.,* **367,** 39–51.

Ritsema, J., Van Heijst, H., Woodhouse, J. & Deuss, A., 2009. Long-period body wave traveltimes through the crust: implication for crustal corrections and seismic tomography, *Geophys. J. Int.,* **179**(2), 1255–1261.

Roberts, D., 2003. The Scandinavian Caledonides: event chronology, palaeogeographic settings and likely modern analogues, *Tectonophysics,* **365**(1-4), 283–299.

Rohrman, M. & van der Beek, P., 1996. Cenozoic postrift domal uplift of North Atlantic margins: an asthenospheric diapirism model., *Geology,* **24,** 901–904.

Rohrman, M., Van Der Beek, P.A., Van Der Hilst, R.D. & Reemst, P., 2002. Timing and mechanisms of North Atlantic Cenozoic uplift: evidence for mantle upwelling, *Geol. Soc. Lond. Spec. Publ.,* **196,** 27–44.

Shapiro, N. & Ritzwoller, M., 2002. Monte-Carlo inversion for a global shear-velocity model of the crust and upper mantle, *Geophys. J. Int.,* **151**(1), 88–105.

Shapiro, N. & Ritzwoller, M., 2004. Thermodynamic constraints on seismic inversions, *Geophys. J. Int.,* **157**(3), 1175–1188.

Shomali, Z., Roberts, R.G. & Pedersen, L.B., 2006. Lithospheric structure of the Tornquist Zone resolved by nonlinear P and S teleseismic tomography along the TOR array, *Tectonophysics,* **416**(1), 133–149.

Shomali, Z.H. & Roberts, R.G., 2002. Non-linear body wave teleseismic tomography along the TOR array, *Geophys. J. Int.,* **148**(3), 562–574.

Sigloch, K., 2008. Multiple-frequency body-wave tomography, *PhD thesis,* Princeton University.

Simons, F.J. *et al.*, 2011. Solving or resolving global tomographic models with spherical wavelets, and the scale and sparsity of seismic heterogeneity, *Geophys. J. Int.,* **187**(2), 969–988.

Sobolev, S.V., Zeyen, H., Stoll, G., Werling, F., Altherr, R. & Fuchs, K., 1996. Upper mantle temperatures from teleseismic tomography of French Massif Central including effects of composition, mineral reactions, anharmonicity, anelasticity and partial melt, *Earth planet. Sci. Lett.,* **139**(1), 147–163.

Sørensen, K., 1986. Danish Basin subsidence by Triassic rifting on a lithosphere cooling background, *Nature,* **319,** 660–663.

Stratford, W. & Thybo, H., 2011. Seismic structure and composition of the crust beneath the southern Scandes, Norway, *Tectonophysics,* **502**(3), 364–382.

Svenningsen, L., Balling, N., Jacobsen, B., Kind, R., Wylegalla, K. & Schweitzer, J., 2007. Crustal root beneath the highlands of southern Norway resolved by teleseismic receiver functions, *Geophys. J. Int.,* **170**(3), 1129–1138.

Sweldens, W., 1996. The lifting scheme: a custom-design construction of biorthogonal wavelets, *Appl. Computat. Harmonic Anal.,* **3**(2), 186–200.

Thybo, H., 2001. Crustal structure along the EGT profile across the Tornquist Fan interpreted from seismic, gravity and magnetic data, *Tectonophysics,* **334**(3), 155–190.

Torsvik, T.H., Smethurst, M.A., Burke, K. & Steinberger, B., 2008. Long term stability in deep mantle structure: evidence from the 300 Ma Skagerrak-Centered Large Igneous Province (the SCLIP), *Earth planet. Sci. Lett.,* **267**(3), 444–452.

Trampert, S. & Snieder, R., 1996. Model estimations biased by truncated expansions: possible artifacts in seismic tomography, *Science,* **271,** 1257–1260.

Van Wijk, J., Baldridge, W., Van Hunen, J., Goes, S., Aster, R., Coblentz, D., Grand, S. & Ni, J., 2010. Small-scale convection at the edge of the Colorado Plateau: implications for topography, magmatism, and evolution of Proterozoic lithosphere, *Geology,* **38**(7), 611–614.

VanDecar, J. & Crosson, R., 1990. Determination of teleseismic relative phase arrival times using multi-channel cross-correlation and least squares, *Bull. seism. Soc. Am.,* **80**(1), 150–169.

Wawerzinek, B., Ritter, J. & Roy, C., 2013. New constraints on the 3D shear wave velocity structure of the upper mantle underneath Southern Scandinavia revealed from non-linear tomography, *Tectonophysics,* **602,** 38–54.

Weidle, C. & Maupin, V., 2008. An upper-mantle S-wave velocity model for Northern Europe from Love and Rayleigh group velocities, *Geophys. J. Int.,* **175**(3), 1154–1168.

Weidle, C. *et al.*, 2010. MAGNUS—a seismological broadband experiment to resolve crustal and upper mantle structure beneath the Southern Scandes Mountains in Norway, *Seismol. Res. Lett.,* **81**(1), 76–84.

Wessel, P. & Smith, W., 1998. New improved version of the generic mapping tools released, *EOS, Trans. Am. geophys. Un.,* **79**(33), 579.

Yang, T. & Shen, Y., 2006. Frequency-dependent crustal correction for finite-frequency seismic tomography, *Bull. seism. Soc. Am.,* **96**(6), 2441–2448.

Yuan, Y.O. & Simons, F.J., 2014. Multiscale adjoint waveform-difference tomography using wavelets, *Geophysics,* **79**(3), WA79–WA95.

Zhu, H., Bozdağ, E., Peter, D. & Tromp, J., 2012. Structure of the European upper mantle revealed by adjoint tomography, *Nature Geosci.,* **5**(7), 493–498.

Zhu, H., Bozdağ, E., Duffy, T.S. & Tromp, J., 2013. Seismic attenuation beneath Europe and the North Atlantic: implications for water in the mantle, *Earth planet. Sci. Lett.,* **381,** 1–11.

Zielhuis, A. & Nolet, G., 1994. Deep seismic expression of an ancient plate boundary in Europe, *Science,* **265,** 79–79.

SUPPORTING INFORMATION

Additional Supporting Information may be found in the online version of this article:

Figure S1. Synthetic input for a test with two cylinders placed at 100–200 km and 300–400 km depth and diameters of 100 km. The velocity perturbations are −3% for V_{P} and −5% for V_{S}. Upper left map shows location of profiles and grid discretisation.
Figure S2. Recovered P-wave model using the 3D multiscale parameterisation in a test with the synthetic model shown in Supplementary Fig. 1.
Figure S3. Recovered S-wave model using the 3D multiscale parameterisation in a test with the synthetic model shown in Supplementary Fig. 1.
Figure S4. Images of dlnVs in the uppermost layers, corresponding to Fig. 13 for P. Input data are the raw travel time residuals without the crustal and topographic corrections from Kolstrup (2015).
Figure S5. As supplementary Fig. 4 but with input data corrected for topography and crustal structure, corresponding to Fig. 14 for P. (http://gji.oxfordjournals.org/lookup/suppl/doi:10.1093/gji/ggv130/-/DC1).